Available online at www.sciencedirect.com

ScienceDirect

Advances in Space Research 68 (2021) 1–24

ADVANCES IN SPACE RESEARCH (a COSPAR publication)

www.elsevier.com/locate/asr

Re-entry analysis of critical components and materials for design-for-demise techniques

Seong-Hyeon Park, Stefano Mischler, Pénélope Leyland *

Ecole Polytechnique Fédérale de Lausanne EPFL, Tribology and Interface Chemistry Group (SCI-STI-SM), Station 12, CH-1015 Lausanne, Switzerland

Received 19 November 2020; received in revised form 19 February 2021; accepted 17 March 2021
Available online 26 March 2021

Abstract

The concern caused by the rising population of space debris has increased. One of the recommended mitigation measures is the safe re-entry disposal either in a controlled or uncontrolled manner. Performing a controlled re-entry, where the spacecraft is guided down to impact in a designated zone such as the ocean or a non-populated area, complies with the mitigation standards. However, it has limitations in terms of the cost of developing and ensuring reliability of a system. Therefore, an uncontrolled re-entry can be preferred as a simpler and cheaper alternative for the disposal of space debris. To reduce the casualty area of the surviving fragments, design-for-demise techniques have been proposed. From the point of view of the design-for-demise techniques, it is significant to identify and investigate the critical components that are directly related to the casualty risk. In this paper, re-entry survivability analysis of critical components has been conducted to identify the most critical ones and to understand the effects of uncertainties on casualty risk. The material properties within elements such as the propellant tanks, balance masses and payloads that can be critical components are crucial parameters. The initial conditions, relative sizes, and aerodynamic forces are also significant. In the view of engineering design, either a change of the material or a mass/size reduction is recommended to demise the components. Monte Carlo simulations are performed to evaluate the sensitivity.

Keywords: Re-entry survivability; Spacecraft component materials; Design-for-Demise; Critical components; Space debris

1. Introduction

In the past two decades, the concern caused by the rising population of space debris has increased. Nonfunctional satellites, abandoned launch vehicle stages, mission-related debris, and fragments generated by collisions and/or explosions of spacecraft has polluted the space environment in the form of space debris (Trisolini et al., 2018a; Trisolini et al., 2018b). Space debris in the Earth's orbit is now recognised as a serious environmental problem in space. Collisions with even small space debris against other objects such as satellites or even a space station can involve high kinetic energy and produce a large number of smaller debris which could cause disaster (Sato, 1999). Re-entering debris involve high speeds (even more than 8 km/s) that can break-up into smaller parts, which could lead to dramatic collisions along the trajectory and also present a serious risk of ground impact if not consumed beforehand.

The major national organisations of the space faring nations have proposed a series of debris mitigation measures to protect the space environment (Kato, 2001). One of the recommended mitigation measures is the safe re-entry disposal either in a controlled or uncontrolled manner in order to remove debris from orbit. Although most spacecrafts may completely burn up during re-entry,

* Corresponding author.
E-mail addresses: seong-hyeon.park@epfl.ch, shpark2306@gmail.com (S.-H. Park), stefano.mischler@epfl.ch (S. Mischler), penelope.leyland@epfl.ch (P. Leyland).

https://doi.org/10.1016/j.asr.2021.03.019
0273-1177/

surviving ones can pose a risk to people and property on the ground. Regarding the risk, space debris mitigation standards have been established specifying an upper limit for the acceptable casualty expectancy for a re-entry as 0.0001 (O'Connor, 2008; Klinkrad and Bohlmann, 2008). Compliance with this requirement can be achieved performing a controlled re-entry, where the spacecraft is guided to impact in a designated zone such as an ocean or unpopulated areas (Trisolini et al., 2018a). However, controlled re-entries have some limitations in terms of the cost of developing, launching, and ensuring reliability of a system (Kärräng et al., 2019). Therefore, uncontrolled re-entry is preferred as a simpler and cheaper alternative for the disposal of a space object at the end of its operational lifetime (Waswa and Hoffman, 2012; Waswa et al., 2013). The way to comply with the regulation on the casualty risk expectation during an uncontrolled re-entry is to reduce the casualty area of the surviving fragment. Intentionally designing spacecraft to meet the casualty risk constraint is known as design-for-demise (Kärräng et al., 2019). Selection of the materials, the use of multiple layers, the optimisation of the shape, size and thickness of the components, rearranging the components, optimise heat transfer, minimise required heat, etc. are included in the design-for-demise strategies on the system and the component level.

According to the previous literature (Trisolini et al., 2018b; Kärräng et al., 2019; Riley et al., 2015), propellant tanks, reaction wheels, magnetic torquers, and payloads are regarded as critical components for re-entry analysis. From the point of view of the design-for-demise techniques, it is significant to identify and investigate the critical components because they are directly related to the casualty area of the surviving fragments of a spacecraft. The destruction of a re-entering spacecraft should also be considered. Most of the critical components are located inside the satellite, and they are usually exposed to atmospheric re-entry by a break-up. Even though the break-up is known to usually occur in a range of altitude between 75 and 85 km, such uncertainties can significantly affect the initial conditions and dynamic motions of the critical components (Park and Park, 2018; Park and Park, 2019).

The objective of present paper is to analyse specific critical components in terms of re-entry casualty risk, particularly investigating the effects on size, shape, material, and re-entry environment. To evaluate the re-entry casualty risk of critical components, an object-oriented re-entry tool is used to simulate the conditions experienced by the components. It allows users to run fast and extensive parametric and statistical analyses with various demise scenarios. An uncontrolled re-entry presents many uncertainties in initial conditions, in the atmospheric characteristics, in the object properties, and the break-up mechanisms (Mehta et al., 2017). In this respect, the tool can provide the capability to cope with the uncertainties and help to understand the effect of different parameters on the ground footprint, survivability, and risk analysis. The main motivation for this work is to contribute to the development of design-for-demise techniques to reduce the re-entry casualty risk based on such dedicated simulations.

2. Re-entry analysis

2.1. Re-entry analysis tool

A re-entry analysis tool which is classified under the category of object-oriented tools has been used in this study. The tool has been developed and validated with various existing tools in previous works (Park and Park, 2017; Park et al., 2018; Park et al., 2021). The tool consists of six main modules; namely, trajectory, atmosphere, aerodynamics, aerothermodynamics, thermal analysis, and ablation. The trajectory module calculates a three-degrees-of-freedom (DOF) motion, and the atmosphere module provides the trajectory module with the atmospheric temperature, density, and pressure distribution. The aerodynamic module considers the averaged aerodynamic coefficients of simple-shaped objects (e.g., sphere, cylinder, box, or a flat plate) with various motions. The aerothermodynamic module calculates the net heating rate to an object. The thermal analysis module computes the surface temperature and inner temperature of an object by interacting with the aerothermodynamic module. Finally, the ablation module determines whether the object would demise or not, using the results obtained by the aerothermodynamics and thermal analysis modules. The process continues until the object is either completely melted or it reaches the ground (Park and Park, 2017; Park et al., 2018).

2.1.1. Trajectory and atmosphere modules

In the trajectory module, a three-degrees-of-freedom (DOF) motion is calculated by using the equations derived in an Earth-fixed reference frame assuming a rotating Earth sphere. Gravity and aerodynamic forces are considered in this module assuming that all objects are mass points and lift is neglected. The equations are solved using a fourth order Runge–Kutta numerical integration scheme, as given below (Weiland, 2010).

$$\dot{r} = V sin\gamma \tag{1}$$

$$\dot{\theta} = \frac{V cos\gamma cos\chi}{r cos\phi} \tag{2}$$

$$\dot{\phi} = \frac{V cos\gamma sin\chi}{r} \tag{3}$$

$$\frac{dV}{dt} = -\frac{1}{m}D - g sin\gamma + \omega^2 r cos^2\phi (sin\gamma - cos\gamma tan\phi sin\chi) \tag{4}$$

$$V\frac{d\gamma}{dt} = \frac{1}{m}L - g cos\gamma + \frac{V^2}{r}cos\gamma + 2\omega V cos\phi cos\chi + \omega^2 r cos^2\phi (cos\gamma + sin\gamma tan\phi sin\chi) \tag{5}$$

$$V\frac{d\chi}{dt} = -\frac{V^2}{r}cos\gamma cos\chi tan\phi + 2\omega V(tan\gamma cos\phi sin\chi - sin\phi) - \frac{\omega^2 r}{cos\gamma}sin\phi cos\phi cos\chi \quad (6)$$

where r is the magnitude of position vector, θ is the longitude angle, ϕ is the latitude angle, V is the velocity, γ is the flight path angle, χ is the azimuth angle, ω is the atmospheric rotational speed, m is the mass, and g is the gravity. L and D represent lift and drag, respectively.

The atmosphere module produces the atmospheric temperature, density, and pressure depending on the altitude. The 1976 U.S. Standard Atmosphere Model is mainly used in this module. Aside from this, several atmosphere models such as the NRLMSISE-00 can also be used in this module (Park and Park, 2017).

2.1.2. Aerodynamic module

In the aerodynamic module, the averaged drag coefficients of simple-shaped objects such ass sphere, cylinders, boxes, or flat plates are calculated for free molecular, transitional, and continuum flow regimes as a function of the Knudsen number (Kn) (Park and Park, 2017; Cropp, 1965; Rochelle et al., 1997; Carnà and Bevilacqua, 2019). The Knudsen number is defined by,

$$Knudsen\ number = \frac{\lambda}{L} = \frac{k_B T}{\sqrt{2}d^2 pL} \quad (7)$$

where λ is the mean free path, L is the representative physical length scale, k_B is the Boltzmann constant, and d is the diameter of a particle. T and p represent the temperature and pressure, respectively. Continuum flow and free molecular flow regimes correspond to small (Kn $<$ 0.01) and large (Kn $>$ 10) Knudsen numbers, respectively. The drag coefficients are computed using the modified Newtonian flow theory in the continuum flow regime, while the coefficients are commonly calculated using the Schaaf-Chambre method in the free molecular flow regime (Kärräng et al., 2019; Anderson, 2006). In the transitional flow regime, the aerodynamic coefficients are calculated using a bridging function which connects free molecular to continuum flow regimes. In the present study, the bridging function presented by Rochelle et al. is used (Rochelle et al., 1997). More details on aerodynamic coefficients can be found in (Trisolini et al., 2018a; Cropp, 1965).

2.1.3. Aerothermodynamic module

The net heating rate to the re-entry object is calculated in the aerothermodynamic module. It consists of the convective heating rate, oxidation heating rate, and re-radiation heating rate. While the convective heating rate and oxidation heating rate increase the net heating rate, the re-radiation heating rate decreases it. The net heating rate can be expressed as follows.

$$q_{net} = q_{conv} + q_{ox} - q_{rr} \quad (8)$$

where q_{net} is the net heating rate to the surface per unit time and area (W/m^2), q_{conv} is the convective heating rate, q_{ox} is the oxidation heating rate, and q_{rr} is the re-radiation heating rate. The convective heating rate is calculated as the product of the wall enthalpy ratio and the cold wall convective heating rate by considering an actual hot wall (Rochelle et al., 1997). The cold wall convective heating rate can be obtained as the stagnation-point heating rate multiplied by a factor, F, to provide the average heating the object. The details on the averaging factors can be found in (Trisolini et al., 2018a; Trisolini et al., 2018b; Cropp, 1965).

In line with the aerodynamic module, the free molecular, transitional, and continuum flow regimes are considered for the stagnation-point heating rate. For the free molecular flow regime, the stagnation enthalpy can be approximated as $0.5V_\infty^2$ at high Mach number hypersonic speeds. Then, the stagnation-point heating rate can be calculated as the product of the stagnation enthalpy, mass flow rate, and thermal accommodation coefficient (Klett, 1964; Sim and Kim, 2011):

$$q_{stag} = \frac{\alpha \rho V_\infty^3}{2} \quad (9)$$

where α is the thermal accommodation coefficient, and ρ and V_∞ denote the air density and velocity, respectively. The thermal accommodation coefficient is commonly assumed to be 0.9 because the coefficients for most of metals and ceramics are in between 0.8 and 1.0 (Cropp, 1965).

For the continuum flow regime, Goulard's heat transfer theory is used to calculate the stagnation-point heating rate (Goulard, 1958). With this theory, the flow is assumed to be in a state of chemically frozen in the boundary layer. The total heating rate consists of two main parts: conductive heating rate, which is manifested by the temperature gradient, and diffusive heating rate, which results from surface catalytic recombination. The total heating rate can hence be expressed as,

$$q_{stag} = 0.664(\beta \mu_e \rho_e)^{1/2} \overline{Pr}_w^{-2/3} h_e \left[1 + \left(Le^{2/3}\varphi - 1\right)\frac{h_R c_e}{h_e}\right] \quad (10)$$

$$\varphi = \frac{1}{1 + \frac{0.47 Sc^{-2/3}(2\beta\mu_e\rho_e)^{1/2}}{\rho_w k_w}} \quad (11)$$

The subscripts e and w represent the boundary layer edge and wall, respectively. β is the velocity gradient ($\beta = du_e/dx$, where u_e is the velocity at boundary layer edge and x is the distance along the wall from the stagnation-point), μ is the viscosity, $\overline{Pr}_w$ is the Prandtl number (where $\overline{Pr}_w$ was held constant at 0.71), h is enthalpy, Le is the Lewis number ($Le = \overline{Pr}_w/Sc$), h_R is the heat of recombination (where the standard heat of recombination h_R, 8089 cal/gr for nitrogen and 3686 cal/gr for oxygen, was used), c is the atomic mass fraction (where c is changed according to re-entry trajectory), Sc is the Schmidt number

($Sc = 0.485$), k_w is the catalytic velocity. φ describes the catalytic effect in the heat transfer formulation through the catalytic velocity. The catalytic velocity depending on the catalytic recombination probability can be expressed as,

$$k_w = \frac{\gamma}{4}\sqrt{\frac{8k_B T_w}{\pi m}} \tag{12}$$

where γ is the catalytic efficiency, k_B is the Boltzmann's constant, T_w is the wall temperature, and m is the atom mass.

The stagnation-point heating rate can be calculated using the Stanton number. For the transition flow regime, bridging functions for the Stanton number (St) are used to connect the free molecular (St_{fm}) and continuum flow regimes (St_{cont}). The following equation is used based on the previous literature and resumed in (Lips and Fritsche, 2005).

$$St_{trans} = \frac{St_{cont}}{1 + St_{cont}/St_{fm}} \tag{13}$$

$$St = \frac{q_{stag}}{0.5\rho V_\infty^3} \tag{14}$$

The oxidation heating rate is calculated using the equation presented by Cropp (Cropp, 1965). The heat loss from the hot outer surface due to re-radiation is computed by means of the Stephan–Boltzmann equation with the emissivity and wall temperature of the object. It is expressed as follows,

$$q_{rr} = \varepsilon\sigma T_w^4 \tag{15}$$

where ε is the material emissivity and σ is the Stephan–Boltzmann constant (5.67×10^{-8} W/m^2-K^4). The whole surface area contacting the surrounding air is used as the reference area.

2.1.4. Thermal analysis and ablation modules

The thermal analysis module predicts the surface temperature and inner temperature of the object. In this module, a 1-D heat conduction model ("thermal math model") is used assuming that the heat is conducted in the radial direction. An onion model for the object is made, each layer having a certain thickness, assuming constant temperature per layer. The surface temperature and each layer is determined using the net heat rate provided by the aerothermodynamic module. For the hollow objects, (for example a hollow cylinder), the innermost layer is assumed to be adiabatic. The temperature is computed using a Forward Time Central Space (FTCS) finite difference method (Park and Park, 2017). For a spinning sphere, the differential equation is given in spherical coordinates as:

$$\rho C_p \frac{\partial T}{\partial t} = \frac{1}{r^2}\frac{\partial}{\partial r}\left(kr^2\frac{\partial T}{\partial r}\right) \tag{16}$$

where C_p is the specific heat, t is the time, r is the distance in radial direction, and k is the thermal conductivity. For each interior layer, the temperature is calculated using the following finite difference relationships for the absorbed heat (Q),

$$\begin{aligned} Q_{in} &= G_j\left(T_{j+1} - T_j\right)\triangle t \\ Q_{out} &= G_{j-1}\left(T_j - T_{j-1}\right)\triangle t \\ T_i &= T_{i-1} + \tfrac{Q_{in}-Q_{out}}{m_j C_{p,j}} \end{aligned} \tag{17}$$

where the subscripts j and i denote layer index and time index, respectively. m_j is mass of j^{th} layer. G is the radial conductor and is defined by the expression:

$$G = \frac{4\pi k}{\frac{1}{r_1} - \frac{1}{r_2}} \tag{18}$$

The surface temperature can be obtained using the temperature of the outermost layer and the net heating rate (q_{net}). The equation is written as,

$$T_w = \frac{q_{net} \times A_w}{G} + T_{old} \tag{19}$$

where A_w and T_{old} are the surface area and temperature of the outermost layer, respectively (Park and Park, 2017; Kelley and Rochelle, 2012).

The ablation module determines whether the outer layer of the object is removed or not. After the absorbed heat reaches the heat of ablation of the outer layer, the temperatures are fixed at the melting temperature and the layer is eliminated by an assumed shear force, and the net heating rate is applied to the next layer. As a result, the changed mass, size, and ballistic coefficient of the object are applied to the other modules. The process continues iteratively until all the layers are melted or the object reaches the ground (Rochelle et al., 1997; Sim and Kim, 2011).

$$Q_{absorbed,j} > H_{ablation,j} = m_j\left(h_{f,j} + \int_{T_{init,j}}^{T_{melt,j}} C_{p,j}(T)dT\right) \tag{20}$$

where $Q_{absorbed,j}$ is the total absorbed heat, $H_{ablation,j}$ is the heat of ablation, $h_{f,j}$ is the heat of fusion for the material, $T_{init,j}$ is the initial temperature, $T_{melt,j}$ is the melting temperature for the material, and $C_{p,j}$ is the specific heat for the material of j^{th} layer (Kelley and Rochelle, 2012). In this paper, the specific material properties of the components: thermal conductivity, heat of fusion, specific heat, density, and emissivity are constant per temperature step using the data from (Liou et al., 2015; MatWeb, 2015).

2.2. On-ground casualty risk estimation

The re-entry casualty risk is defined and estimated based on the previous literature (Kärräng et al., 2019; Riley et al., 2015; Klinkrad, 2010). The size, mass, and impact velocity of surviving fragments need to be determined to conduct the risk estimation. If their kinetic impact energy is above 15 J, the fragments are considered to be hazardous. The individual casualty area is computed by the cross-section of the impacting fragment and a human cross-section, and the total casualty area is expressed as the sum of the

casualty cross-section for all the hazardous fragments (Kärräng et al., 2019):

$$A_c = \sum_i^N \left(\sqrt{A_h} + \sqrt{A_i}\right)^2 \quad (21)$$

where A_c is the total casualty area of the surviving fragments, A_h is the average cross-section of a human body ($\sim$0.36 m^2), and A_i is the average cross-section of the surviving fragment i. According to this equation, the total casualty area can be reduced by limiting the number of surviving fragments or limiting the size of fragments. Reducing the kinetic energy of the fragments can be also an alternative for risk reduction. The critical components are directly related to the casualty area because most of the surviving fragments are included in the critical components. Therefore, the identification and analysis of the critical components for the re-entry casualty risk are significant for the development of design-for-demise techniques.

3. Identification of critical components

According to the previous literature (Trisolini et al., 2018b; Kärräng et al., 2019; Riley et al., 2015), propellant tanks, reaction wheels, balance masses, magnetic torquers, and payloads are regarded as critical components for re-entry analysis. Particularly, among them, the propellant tanks and pressure spheres have been most commonly found on the ground. Components made of materials with a high heat of fusion or that are well protected within the spacecraft can also be potential critical components. In this section, these critical components are introduced and investigated. Based on simplified models using primitive shapes like spheres, boxes, cylinders, and flat plates (solid/hollow), they will be analysed considering the uncertainties that directly affect the demisability in the following Section 4.

3.1. Propellant tank

Propellant tanks are used to store propellant and are usually under high pressure. They are typically large components of satellites and their weight are between 5 and 60 kg (Riley et al., 2015). They are commonly identified as critical ground casualty components and constitute the majority of retrieved re-entered objects because these components are usually made of titanium alloys (e.g. Ti-6Al-4V) which have not only a high heat of fusion but also a high melting temperature. Moreover, the heating rate due to re-entry is proportional to the ballistic coefficient. The propellant tanks are usually modelled as a hollow sphere which has a large frontal area for a reasonably low mass, so they are more likely to survive with a relatively low ballistic coefficient.

Table 1 lists vendor supplied information for the net volume V, Maximum Expected Operating Pressure (MEOP), burst pressure p_b, mass m, diameter d and height h. The tanks include spherical, elliptical or cassini domes with or without variable length cylindrical intersections. The abbreviated terms Sph, Sph + C, and Cas + C denote the spherical, spherical/elliptical domes with cylindrical intersection, and cassini domes with cylindrical intersection, respectively, (Radtke, 2004; Radtke, 2005). In the simulations, for the tanks with cassini domes, a simple cylinder is assumed when the height is less than the diameter.

Fig. 1 shows the schematic of the tank. The wall thickness of the tank can be determined by the mass and the surface of the wall. In the case of the spherical domes with cylindrical intersections, the thickness is given by

$$e = \frac{m}{\rho S}, \quad S = \pi\left[d^2 + d(h-d)\right] \quad (22)$$

In the case of the cylinder, it is given by

$$e = \frac{m}{\rho S}, \quad S = \pi\left[dh + \frac{d^2}{2}\right] \quad (23)$$

3.2. Reaction wheel

Reaction wheels (RW) are elements of the Attitude Determination and Control System (ADCS), which is a crucial subsystem of a spacecraft. They fundamentally provide momentum storage and reactive torques for disturbance reduction. These attitude control systems are operated by relying on the conservation of angular momentum and hence accumulate the angular momentum from the external torques. If the external torques does not work periodically, other attitude control systems that provide momentum dumping such as magnetic torquers or thrusters are used. For three-axis control, reaction wheels are mounted along at least three directions, with extra wheels providing redundancy to the attitude control system. The reaction wheels are known to be the critical components because they are usually made of dense and strong materials such as stainless steel.

Table 2 provides a non-exhaustive list of reaction wheels that can be found on the internet for commercial use on small to medium sized spacecraft. This table shows vendor supplied information for the diameter d, height h, mass m, nominal torque T, maximum angular momentum L and maximum angular velocity $\omega_{\max}$.

3.2.1. Reverse engineering

Fig. 2 shows a generic reaction wheel geometry. The reaction wheel consists of three main sub-elements: (1) reaction wheel, (2) hardware such as the housing, bearings and the central axis, (3) an electric motor.

The approximate sub-element sizing is determined by performing reverse engineering of the element. At first, it is assumed that the angular momentum L is mostly due to the outer ring of the free wheel.

$$L = I\omega, \quad I = k_w m_w r_w^2 \quad (24)$$

Table 1
Commercially available propellant tanks (EADS Astrium GmbH, 2015).

Shape	V (dm^3)	MEOP (bar)	p_b (bar)	m (kg)	d (mm)	h (mm)	S (m^2)	e (mm)
Sph	58.0	26.0	52.0	8.5	480.0	480.0	0.72	2.66
Sph	218.0	22.0	33.0	11.0	760.0	760.0	1.81	1.37
Sph	104.0	24.6	49.2	6.4	586.0	586.0	1.08	1.34
Sph + C	176.5	24.6	49.3	13.5	600.0	896.0	1.69	1.81
Sph + C	177.0	24.0	48.0	15.0	589.0	899.0	1.66	2.04
Cas + C	198.0	22.0	44.0	17.5	753.0	651.5	1.54	2.57
Sph	235.0	22.0	44.0	16.0	756.0	756.0	1.79	1.61
Cas + C	282.0	22.0	44.0	21.0	753.0	643.5	1.97	2.41
Cas + C	331.0	19.5	29.3	22.7	753.0	953.5	2.26	2.28
Cas + C	1108.0	19.5	29.3	49.0	1146.0	1087.0	4.94	2.24
Sph + C	745.0	22.5	35.9	39.5	693.0	2335.0	5.08	1.76
Sph	769.0	17.5	35.0	31.7	1153.0	1153.0	4.18	1.72
Cas + C	1207.0	19.5	29.3	52.5	1146.0	1456.0	5.24	2.27
Cas + C	1450.0	19.5	29.3	61.0	1141.0	1683.0	6.03	2.29

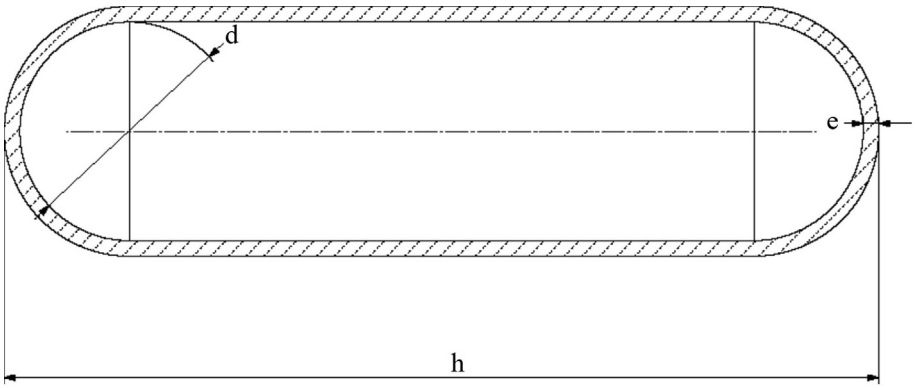

Fig. 1. Section view of the spherical domes with cylindrical intersections.

Table 2
Commercially available reaction wheels (VECTRONIC Aerospace GmbH, 2020; Collins Aerospace, 2020; Blue Canyon Technologies, 2020; Haslehurst and Lewis, 2011; Honeywell Aerospace Electronic Systems, 2020).

Supplier	Model	d (mm)	h (mm)	m (kg)	T (mNm)	L (Nms)	ω (rpm)
Vectronic Aerospace	VRW-1	115	77	1.8	25	1	5000
Rockwell Collins	RSI68-170/60	347	124	9.5	170	68	6000
	RSI12-220/45	347	124	6.0	220	12	4500
	RSI18-220/45	347	124	6.5	220	18	4500
	RSI25-220/45	347	124	7.2	220	25	4500
	RSI50-220/45	347	124	9.2	220	50	4500
	RSI30-280/30	347	124	9.2	280	30	3000
Blue Canyon Technologies	RW1	130	80	1.0	100	1	6000
	RW4	150	90	3.1	30	4	6000
	RW6	170	90	3.3	50	6	6000
	RW12	190	110	4.9	100	12	6000
	RW25	210	110	6.9	100	25	6000
	RW50	250	120	9.3	250	50	6000
SSTL	200SP-M (LEO)	240	90	5.2	240	12	5000
Honeywell	HR12	316	159	9.5	200	50	6000
	HR16	418	178	12.0	200	100	6000

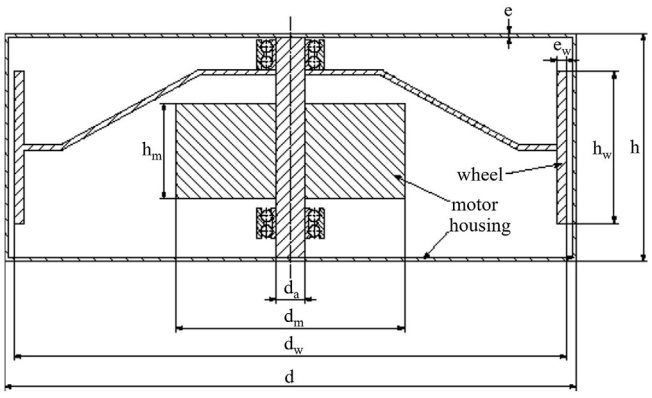

Fig. 2. Section view of the simplified reaction wheel.

where I is the moment of inertia, k_w is the mass fraction of the outer ring to the total wheel mass, m_w is the total reaction wheel mass, and r_w is the wheel radius with $r_w \approx d/2$.

The hardware includes the housing, bearings and central support axis. The housing is modelled as a simple aluminium cylinder which has a diameter d, height h and thickness e. It is assumed that the central axis is modelled as a steel cylinder which has a diameter $d_a = 15$ mm and height h_a = h. Double row deep groove ball bearings (AA7075) are assumed to be with inner and outer diameter of 1.5 mm and 3.6 mm, respectively.

$$m_h = \rho_h e\pi\left(d^2/2 + dh\right) \tag{25}$$

$$m_a = \rho_a \pi d_a^2 h/4 + m_b \tag{26}$$

where m_b is the total bearing mass and is assumed to be 50 g.

The electric motor is more difficult to size since a given torque can be achieved within a range of masses. However, the remaining mass is assumed to be part of the electric motor.

$$m_e = m_w - m_a - m_m - m_h \tag{27}$$

Table 3 shows the calculated sub-elements of the reaction wheel using the reverse engineering.

3.3. Magnetic torquer

Magnetic torquers (MTQ) are part of a satellite subsystem for attitude control, detumbling, and stabilisation built from electromagnetic coils. Thus, they have a similar role to the reaction wheels and are also elements of ADCS. They present an advantage over reaction wheels since they have lower power requirements and do not need moving mechanical parts. However, in general, they are not always able to replace the reaction wheels entirely due to limited available torque and inability to produce torque near the Earth magnetic field. They are often protected within the structure of the spacecraft. Therefore, they can survive to the ground as critical debris since they are exposed to the airflow late during re-entry.

Table 4 lists vendor supplied information for the linear magnetic dipole μ, linear voltage U, linear power P, mass m, length l, and diameter d of commercially available magnetic torquers. Calculated mass and dimension of the sub-elements are also included.

According to the supplier, the total mass consists of both the magnetic core and the wiring. Their mass distribution is between 30 and 70%, respectively. For the dimensions given in Table 4, the magnetic core and wiring were assumed to be 40% of the total mass, respectively. The aluminium housing is 10% of the total mass. The dimensions are computed by assuming that the system can be reduced to an assembly consisting of a concentric cylinder and tubes as shown in Fig. 3. In the following, the subscripts i, c and a refer to the iron core, copper wiring and aluminium housing, respectively.

$$\frac{m_i}{m} = \frac{m_c}{m} = \frac{2m_a}{m} = 0.4 \tag{28}$$

Hence, with the density of iron ρ_i, the iron core diameter d_i is given by

$$d_i = \sqrt{\frac{4 \cdot 0.4m}{\rho_i \pi l}} \tag{29}$$

From this result, the outer diameter of the copper wiring d_c can be deduced as

$$d_c = \sqrt{\frac{4 \cdot 0.4m}{\rho_c \pi l} + d_i^2} \tag{30}$$

Finally, the outer diameter for the aluminium housing is given by

$$d_a = \sqrt{\frac{4 \cdot 0.2m}{\rho_a \pi l} + d_c^2} \tag{31}$$

The obtained outer diameter for the aluminium housing is fairly in agreement with the vendor supplied information within 10% relative errors.

3.4. Balance masses

Regarding the requirements of a spacecraft system, balance masses can be made of various materials (strong materials such as stainless steel; more easily demised materials such as aluminium) or can be differently placed. Although the balance masses are designed completely differently from one spacecraft to another, the larger and internal ones are more likely to survive than the smaller and external ones. Since the balance masses are produced based on the needs of individual missions and are usually not available on the internet, the models used will be assumed and discussed in the following Section 4.

3.5. Payload element

Payload elements are the carrying capacity of a spacecraft, usually measured in terms of weight. Depending on the missions, they can include cargo, flight crew, and scien-

Table 3
Reaction wheel sub-elements.

Model	Wheel[a]			Housing[b]	Axis[c]	Motor		
	m_w (kg)	h_w (mm)	e_w (mm)	m_h (kg)	m_a (kg)	m_m (kg)	d_m (mm)	h_m (mm)
VRW-1	0.77	61.6	3.58	0.340	0.159	0.53	42.3	53.9
RSI68-170/60	4.78	99.2	4.59	2.270	0.226	2.22	65.5	86.8
RSI12-220/45	1.13	99.2	1.08	2.270	0.226	2.38	67.6	86.8
RSI18-220/45	1.69	99.2	1.62	2.270	0.226	2.27	66.1	86.8
RSI25-220/45	2.34	99.2	2.25	2.270	0.226	2.31	66.7	86.8
RSI50-220/45	4.69	99.2	4.50	2.270	0.226	2.02	62.5	86.8
RSI30-280/30	4.22	99.2	4.05	2.270	0.226	2.48	69.0	86.8
RW1*	0.50	64.0	1.99	0.332	0.100	0.07	17.0	56.0
RW4	1.51	72.0	4.60	0.544	0.178	0.87	49.2	63.0
RW6	1.76	72.0	4.74	0.654	0.178	0.71	44.9	63.0
RW12	2.81	88.0	5.56	0.857	0.206	1.02	48.3	77.0
RW25	4.80	88.0	8.58	0.993	0.206	0.90	45.6	77.0
RW50	6.77	96.0	9.32	1.347	0.220	0.96	45.1	84.0
200SP-M	2.12	72.0	4.05	1.108	0.178	1.80	68.9	63.0
HR12	4.24	127.2	3.48	2.203	0.276	2.78	64.7	111.3
HR16	4.85	142.4	2.69	3.557	0.303	3.29	66.5	124.6

a The wheel (A316) diameter is approximately the total diameter ($d_w \approx d$)
b The housing (AA7075) dimensions match the component dimensions (thickness = 2.5 mm)
c The axis (A316) length matches the component height and diameter $d_a = 15$ mm
* Housing 2 mm thick and $d_a = 10$ mm

Table 4
Commercially available magnetic torquers.

Model	Vendor information (ZARM Technik, 2020)						Iron core		Copper wiring		Aluminium housing		
	μ (Am^2)	U (V)	p (W)	m (kg)	l (mm)	d (mm)	m_i (kg)	d_i (mm)	d_c (mm)	e_c (mm)	m_a (kg)	d_a (mm)	e_a (mm)
MT2-1	2	5	0.5	0.2	158	15	0.090	9.4	13.0	1.8	0.020	15.1	1.0
MT5-2	5	5	0.8	0.3	240	18	0.135	9.4	12.9	1.8	0.030	15.0	1.0
MT6-2	6	5	0.5	0.3	325	15	0.135	8.0	11.1	1.5	0.030	12.9	0.9
MT10-2-H	10	10	1.0	0.4	330	17	0.158	8.6	11.9	1.7	0.035	13.8	0.9
MT15-1	15	14	1.1	0.4	330	17	0.194	9.6	13.2	1.8	0.043	15.3	1.0
MT30-2	30	13	1.5	1.4	405	29	0.630	15.6	21.5	3.0	0.140	24.9	1.7
MT70-2	70	24	2.6	2.2	581	30	0.990	16.3	22.5	3.1	0.220	26.1	1.8
MT80-1	80	10	3.0	4.1	381	50	1.845	27.5	38.0	5.3	0.410	44.0	3.0
MT80-2	80	28	4.7	2.3	500	32	1.035	17.9	24.8	3.4	0.230	28.7	2.0
MT110-2	110	12	2.9	3.8	600	40	1.710	21.0	29.1	4.0	0.380	33.7	2.3
MT120-1	120	14	2.4	2.7	670	30	1.215	16.8	23.2	3.2	0.270	26.9	1.8
MT140-2	140	10	1.9	5.3	680	43	2.385	23.4	32.3	4.5	0.530	37.4	2.5
MT250-2	250	28	4.8	5.5	883	37	2.475	20.9	28.9	4.0	0.550	33.4	2.3
MT400-2	400	21	the 9.0	11.0	750	56	4.950	32.0	44.3	6.1	1.100	51.3	3.5
MT400-2-L	400	19	11.4	7.8	952	41	3.510	23.9	33.1	4.6	0.780	38.3	2.6

tific instruments such as telescopes, star trackers, electronics, and coolers. Compared to the above mentioned critical components, the payloads show more variation. They may survive to the ground due to their material composition, high mass components, or late exposure (shielding).

The Star trackers are essential elements that assure a spacecraft's accurate attitude in space. They are mainly composed of an Optical Head (OH) and an Electronic Unit (EU). The OH can be subdivided into an optical train, a sensor, and a baffle. The EO can be subdivided into an outer caging with inner electronics. The simplified model is derived from the Astro APS star sensor (Schmidt et al., 2006). The main characteristics and schematic of the star tracker are presented in Table 5 and Fig. 4, respectively.

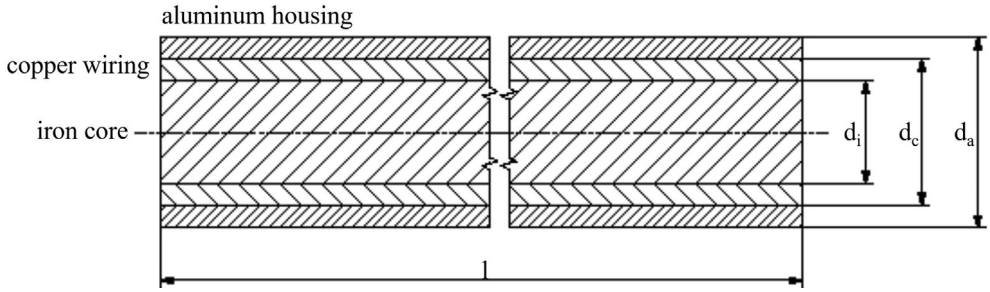

Fig. 3. Schematic of the magnetic torquer model.

Table 5
Astro APS star sensor main element characteristics.

Part	Material	Weight (kg)	Description	Symbol	Value (mm)
Baffle	TiAl6v4	0.170	Diameter	d_b	120
			Height	h_b	140
			Thickness	e_b	1
Optic caging	TiAl6v4	0.065	Diameter	d_o	48
			Height	h_o	50
			Thickness	e_o	2
Optic lens	Radiative-Hard Glass	0.090	Height	h_l	120
Box housing	TiAl6v4	1.130	Width	w_h	120
			Height	h_h	85
			Thickness	e_h	4

4. Results and discussion

The objective of this work is to analyse the factors that influence re-entry casualty risk of critical components, by providing a qualitative analysis. The detailed results are mainly focused on the survivability assessment of the critical components identified after the spacecraft break-up. Thus, this problem can be divided into two main phases (see Fig. 5): (1) re-entry simulation of spacecraft from initial condition to break-up and (2) re-entry survivability assessment of spacecraft critical components after break-up. In the simulations, the uncertainties (such as the re-entry initial conditions, material characteristics, atmospheric properties, heat fluxes, etc.) are considered using Monte Carlo simulations and these results are compared with the nominal results (without uncertainties). One-at-a-time (OAT) and scatter plots are performed by varying only the parameters belonging to a specific category and keeping the others constant, taking uniform or Gaussian (3σ) distributions based on 500–1000 Monte-Carlo simulations.

4.1. Assumptions

The re-entry trajectory and survivability of spacecraft is analysed considering break-up. For the break-up mechanism, it was assumed that fragmentation is not considered and the break-up process is due only to ablation (melting) using a 'parent and child' relationship, a concept by which a single main object such as a spacecraft contains the inner components (Fuentes et al., 2019). After the break-up, each critical component placed within the spacecraft was analysed until it is completely demised or reaches the ground.

Table 6 represents the re-entry initial conditions. Two different uncontrolled re-entries from a Polar Orbit (PO) and an Equatorial Low Earth Orbit (ELEO) were considered, and a controlled re-entry from an orbit characterised by an apogee altitude of 800 km was added for comparison. Table 7 shows the physical properties of the spacecraft. For the spacecraft, 10 different cases made of aluminium AA7075 for simple-shaped objects (5 boxes and 5 cylinders) were considered with the randomly tumbling motion, and their dry mass was between 800 and 4000 kg. The boxes were modelled to have the same width and height. Solar arrays were assumed to remain attached to the spacecraft by increasing the aerodynamic drag, and their break-off altitude was fixed at 92.5 km.

For the critical components (fragments), the tanks, balance masses, and payloads were modelled as single components. The reaction wheels and magnetic torquers were modelled as three separate components: housing, wheel and motor, and housing, wiring and core, respectively. The initial conditions corresponded to the spacecraft break-up. Material properties used for the re-entry analysis were obtained from the NASA Debris Assessment Software 3.0 (DAS 3.0) and MatWeb database (Liou et al., 2015; MatWeb, 2015). For the Monte Carlo simulations (MC), the uncertainties were modelled from the uniform or Gaussian distributions (3σ). The list of the uncertainties is summarised in Table 8. The orbital elements are usually calculated based on a Two-Line Elements set (TLEs). However, they are not perfectly known due to propagator errors, which increase over time. Hence, the uncertainties of orbital elements were assumed based on literature, (Park and Park, 2018; Sanson et al., 2019; San-Juan et al., 2017) and modelled as uniform distributions. According to literature, for example (Sanson et al., 2019), the emissivity uncertainty varies along the trajectory. The reacting flow may alter the surface of the material during a re-entry. The generic metals such as the aluminium usually have an uncertainty of $\pm$ 0.1 depending on the surface polishing, but it can reach $\pm$ 0.2 due to oxidation (Sanson et al., 2019; Barka et al., 2006). For this reason, the

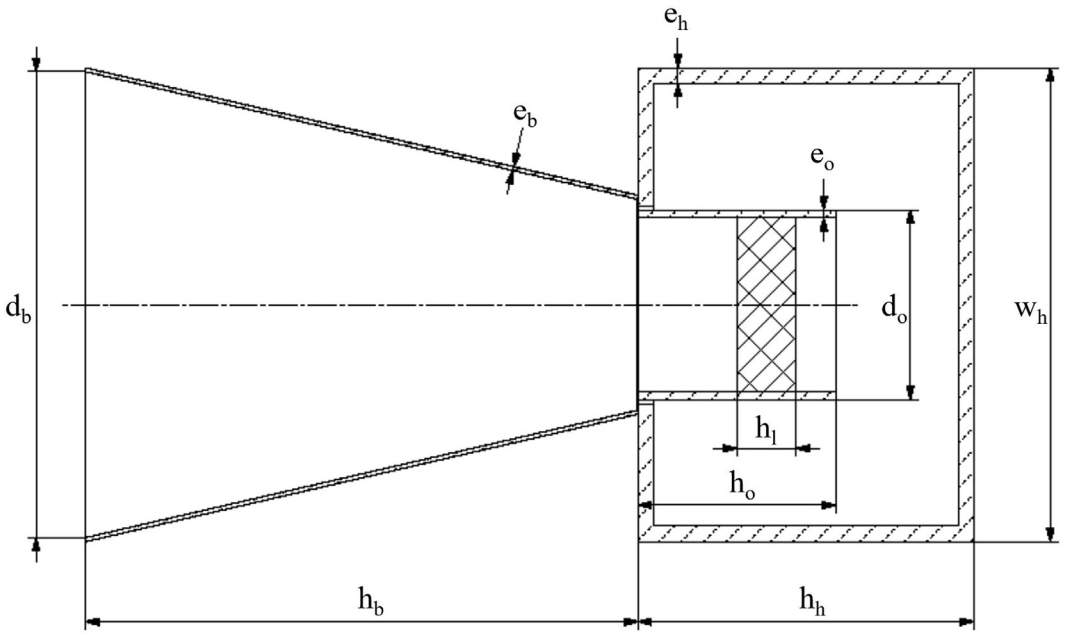

Fig. 4. Section view of the star tracker payload element.

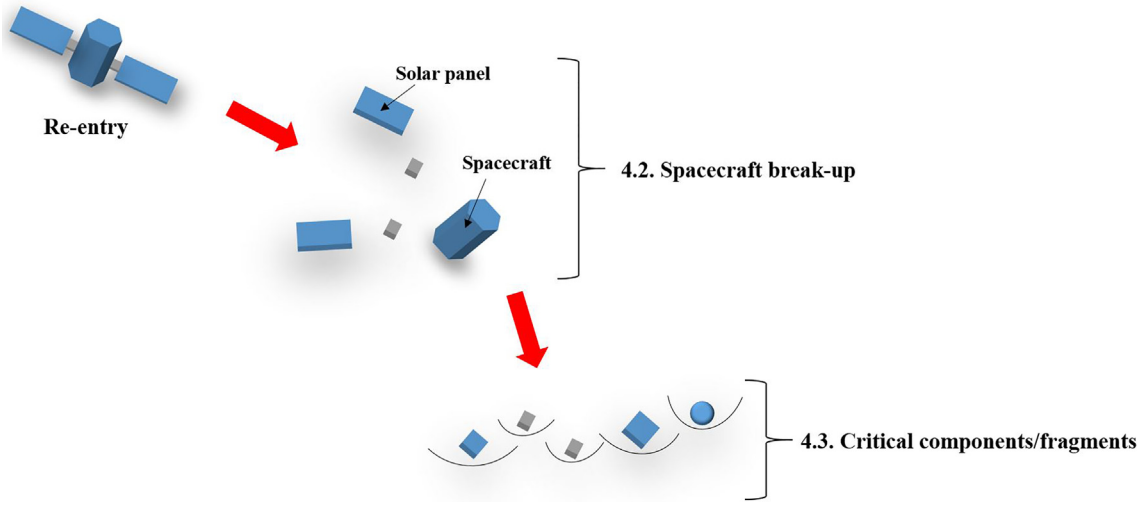

Fig. 5. Summary of the re-entry analysis.

uncertainties were assumed to be ± 0.2 with the uniform distribution for the emissivity. The emissivity is always in the range of from 0 to 1.

4.2. Spacecraft break-up analysis

A spacecraft break-up event is one of the most important factors for the re-entry survivability and trajectory analysis since it can lead to a large discrepancy in the ground footprint and downrange predictions (Park and Park, 2019; Park et al., 2021; Lips and Fritsche, 2005; Wu et al., 2011). According to literature (Wu et al., 2011), the break-up usually occurs at an altitude in the range between 75 and 85 km; however, it could be changed depending on the uncertainties such as the initial conditions, aerodynamics, material characteristics, etc. To identify the range of typical break-up altitudes for the given conditions, nominal simulations (deterministic approach) and Monte Carlo simulations (probabilistic approach) were conducted. The three different re-entry scenarios given in Table 6 were considered: (1) uncontrolled 'shallow' re-entry (Polar Orbit, PO), (2) uncontrolled 'normal' re-entry (Equatorial Low Earth Orbit, ELEO), and (3) controlled 'steep' re-entry (from 800 km) (Mehta et al., 2017). The test models in Table 7 were modelled as a box or cylinder shape. Their masses were 800, 1000, 2000, 3000, and 4000 kg. For the Monte Carlo simulations, the uncertainties were defined in Table 8 in order to estimate

Table 6
Initial conditions.

Orbital elements	Uncontrolled PO	Uncontrolled ELEO	Controlled
Apocentre (km)	145	145	800
Pericentre (km)	145	145	50
Inclination (°)	95	5	95
Argument of periapsis (°)	0	0	0
RAAN (°)	0	0	0
True anomaly (°)	180	180	206

Table 7
Physical properties of the spacecraft.

Parameter	Value				
Shape (–)	Box				
Mass (kg)	800	1000	2000	3000	4000
Length (m)	2	3.55	3.9	6.2	6.5
Width (m)	1.8	2.3	2.6	3.4	4
Shape (–)	Cylinder				
Mass (kg)	800	1000	2000	3000	4000
Length (m)	3	3	3.5	4.5	5.5
Diameter (m)	1.5	2	2.5	2.5	3
Attitude (–)	Randomly tumbling				
External emissivity (–)	0.8				
External panel material (–)	AA7075				
External panel thickness (mm)	3				
Solar array area (m^2)	10				

their effects in the spacecraft break-up altitude, and 500 simulations were performed for each case.

Fig. 6 show the spacecraft break-up altitudes according to re-entry initial orbit elements and masses. Fig. 6(a) and (b) represent the box and cylinder cases, respectively. Both figures show a similar tendency for break-up altitudes. For the boxes, the average nominal break-up altitudes for uncontrolled PO, uncontrolled ELEO, and controlled re-entry scenarios were taken at 82.2, 72.4, and 60.3 km, respectively. For the cylinders, the break-up altitudes were taken at 85.3, 73.6, and 59.0 km, respectively. It can be noted that the break-up altitudes of uncontrolled re-entries are higher than those of controlled re-entries. The controlled re-entries could be considered as a worst case for the demise of inner components because of the late exposure to the atmosphere. This is expected due to the large difference in the respective flight path angles. The flight path angles of uncontrolled re-entries in Table 6 are about 0°, which means that the trajectories maintain a relatively higher altitude for a longer time compared to the controlled re-entry cases before reaching the denser atmosphere. Therefore, the uncontrolled re-entry cases have a longer time to absorb the heat induced from the aerothermodynamics, and consequently this leads to higher break-up altitudes.

In Table 6, the polar orbit has a high inclination angle, while the equatorial low earth orbit has a low inclination. The high inclination orbits lead to higher relative velocities of the re-entry object with respect to the rotating Earth atmosphere. Thus, the deceleration during re-entry takes longer and the absorbed aerothermal heat is higher. Hence, as clearly illustrated in Fig. 6, the break-up altitudes of polar orbit are in overall higher than those of equatorial low Earth orbit. Furthermore, higher break-up altitudes were obtained in the case of the box shape cases compared to the cylinder shape cases although there was only a small difference in the altitudes. The cylinder shapes have a relatively smaller radius, drag coefficient, and cross-sectional area compared to those of the box shapes for the same mass. As the radius and drag coefficient decrease, the stagnation-point heat transfer and ballistic coefficient increase and consequently the demisability increases.

Table 8
Probability distributions of input uncertainties.

No.	Category	Parameter	Type	Spacecraft	Critical components (fragments)
1	Initial condition	Apocentre/Pericentre	Uniform	± 5 km	–
		Inclination	Uniform	± 5°	–
2	Atmosphere	Density	Gaussian	± 10%	± 10%
		Temperature	Gaussian	± 10%	± 10%
3	Size	Mass	Gaussian	± 10%	± 10%
		Length/Width/Diameter	Gaussian	± 10%	± 10%
		External panel thickness	Gaussian	± 10%	–
4	Aerodynamics	Drag coefficient	Uniform	± 10%	± 10%
		Solar arrays break-off	Uniform	± 2.5 km	–
		Solar arrays area	Uniform	± 2.5 m^2	–
5	Aerothermodynamics	Heat flux	Gaussian	± 10%	± 10%
		Accommodation coefficient	Uniform	± 0.1	± 0.1
6	Material property	Emissivity	Uniform	± 0.2	± 0.2
		Melting temperature	Uniform	± 50 K	± 50 K
		Specific heat capacity	Uniform	± 10%	± 10%

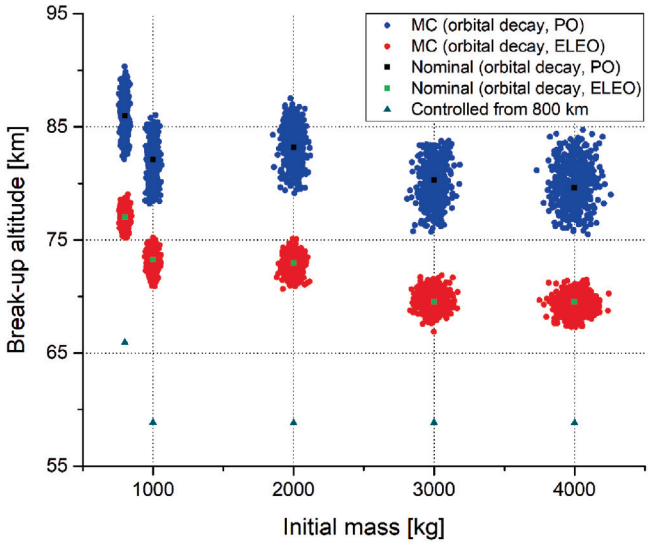

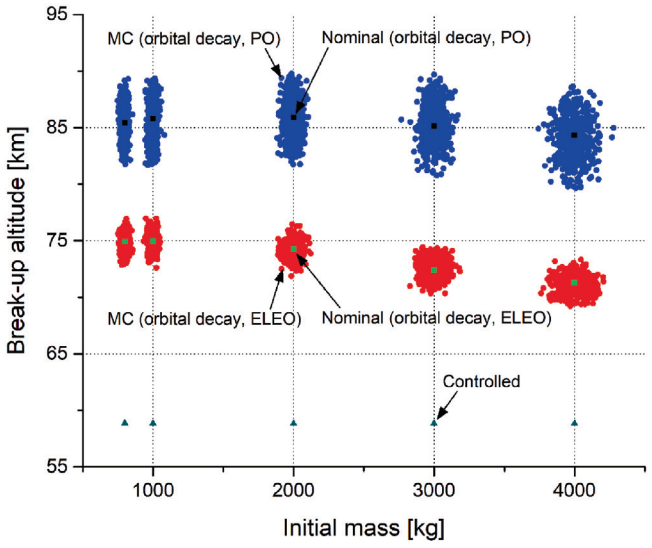

(b) Cylinder

Fig. 6. Spacecraft break-up altitude according to initial conditions for different generic shapes.

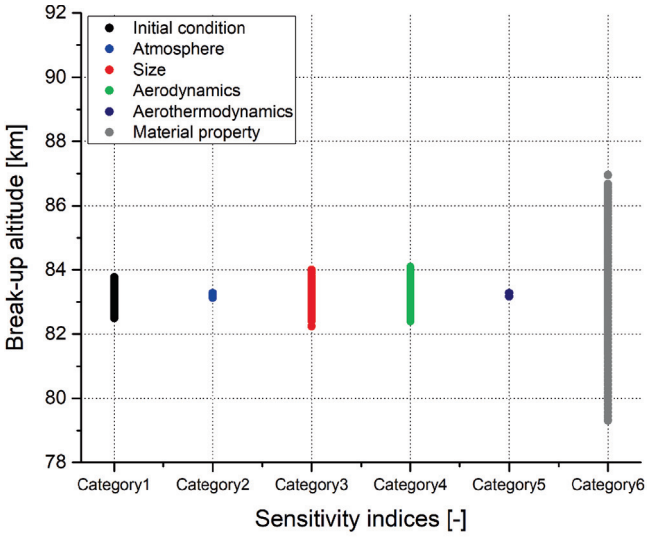

(a) Box

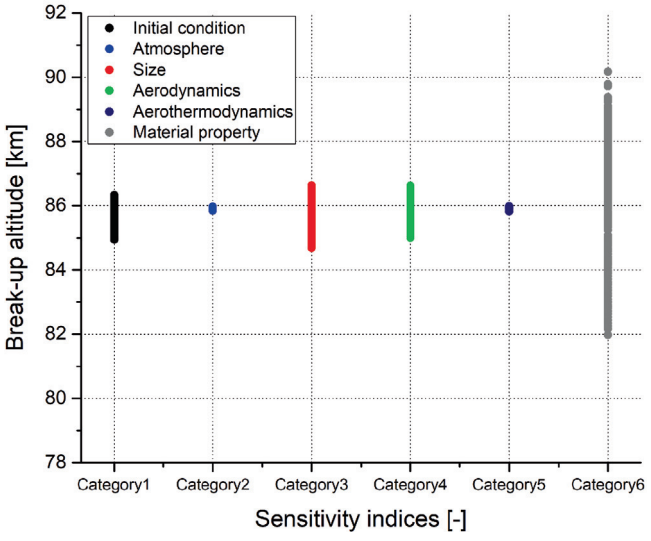

(b) Cylinder

Fig. 7. Influence of uncertainties on break-up altitude for different generic shapes.

To investigate the effect of uncertainties on the break-up altitude, the sensitivity analysis was performed using Monte Carlo simulation, and is presented in Fig. 7. In these simulations, the polar orbit and the case with 2000 kg were used as the initial condition. Table 8 shows the sensitivity indices (categories) and the uncertainty parameters. A total of 6 categories, which are the initial condition, atmosphere, size, aerodynamics, aerothermodynamics, and material property, were considered. It can be noted that the material properties (emissivity, melting temperature, and specific heat capacity) are the most dominant uncertainty parameters in the break-up altitude prediction. The size and aerodynamic factors are also important. Indeed, it is well known that the instantaneous atmospheric density and heat flux have significant effects on the demisability and hence they are directly related to the break-up altitude (Park and Park, 2018; Park and Park, 2017; Rochelle et al., 1997). However, at high altitudes above 80 km, the atmospheric density is very low, whereas the flight velocity is high, hence the radiative cooling is dominant compared to the convective heating rate. These compensating effects are regarded as the main reason for the relatively weak influences. From a spacecraft design point of view, an effective way to modify the break-up altitude could be a careful selection of the spacecraft size and materials since the other uncertainties are not easily controlled.

4.3. Critical components: analyses

Re-entry survivability and ground risk assessment of critical components are investigated. The propellant tanks, reaction wheels, balance masses, magnetic torquers, and payloads discussed in Section 3 were used as the test models. Based on the parent and child relationship assuming the thermal break-up, the initial conditions correspond to the position and velocity of the main break-up of spacecraft. For the uncertainty analysis, based on the same re-entry initial condition, 1000 simulations were performed for each component.

4.3.1. Propellant tanks

The propellant tanks are the most well known critical components of the spacecraft system in terms of survivability during re-entry. Most of these fuel tanks are usually made of titanium alloys (e.g. Ti6 Al-4V) which has not only a high heat of fusion but also a high melting temperature. Thus, with such high survivability materials, they can have a large kinetic energy at ground impact. For the analysis of propellant tanks, the tanks have been divided into two groups depending on their external shape: (1) spherical shape and (2) cylindrical shape.

Table 9 presents the propellant tank cases. In total, 10 different cases (7 spherical cases and 3 cylindrical cases) were considered, and the test cases were modelled based on Table 1. For the spacecraft analysis, the two different re-entry initial conditions (uncontrolled re-entry (Polar Orbit) and controlled re-entry) in Table 6 were used, and the box shaped spacecraft with 800 kg was considered as the parent model (external body). In the Monte Carlo simulations (MC), the uncertainties in Table 8 coming from the applied initial condition, atmospheric model, size, aerodynamic model, aerothermodynamic model, and material properties were considered, and the results were compared with the nominal results. Fig. 8 shows the re-entry survivability results. The demise altitudes are presented in Fig. 8(a). It can be noted that all the cases survived and reach the ground because the estimated final altitudes are less than zero. The ratio of the final mass to the initial mass for cases 1 to 10 is shown in Fig. 8(b). The ratios from

Table 9
Physical properties of propellant tanks.

Case	Shape	Diameter (m)	Length (m)	Mass (kg)	Material
1	Sphere	0.586	–	6.40	Ti-6Al-4V
2	Sphere	0.480	–	8.50	Ti-6Al-4V
3	Sphere	0.760	–	11.00	Ti-6Al-4V
4	Sphere	0.748	–	13.50	Ti-6Al-4V
5	Sphere	0.744	–	15.00	Ti-6Al-4V
6	Sphere	0.756	–	16.00	Ti-6Al-4V
7	Sphere	0.70225	–	17.50	Ti-6Al-4V
8	Cylinder	0.753	0.6435	21.00	Ti-6Al-4V
9	Cylinder	0.693	2.3350	39.50	Ti-6Al-4V
10	Cylinder	1.146	1.0870	49.00	Ti-6Al-4V

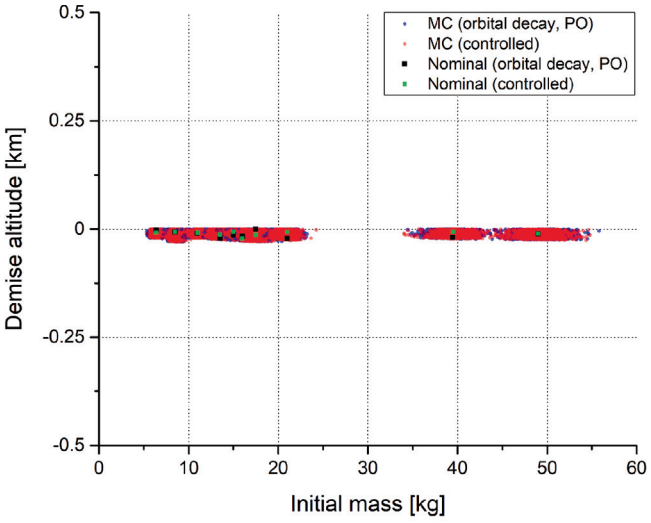

(a) Demise altitude vs. initial mass

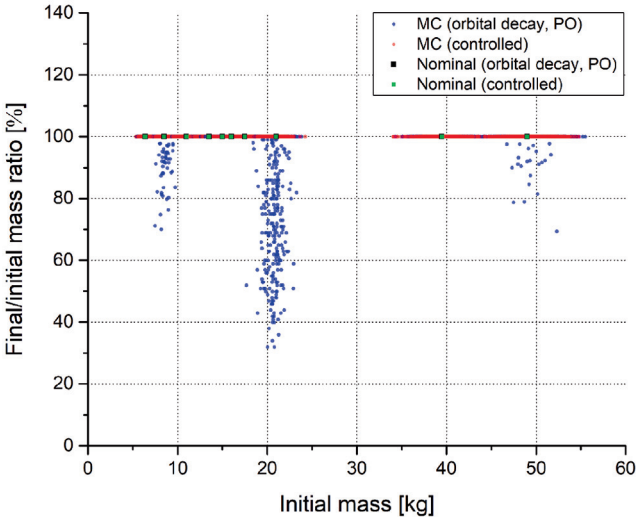

(b) Final/initial mass ratio vs. initial mass

Fig. 8. Survivability results for propellant tanks (cases 1 to 10).

Monte Carlo simulations between controlled re-entry and nominal results are equal to be 100% which means that there is no ablation occurring. However, for the uncontrolled re-entry, ablation occurred in a few cases. The reason is that the inner components from uncontrolled re-entry are exposed to the atmosphere earlier than those of the controlled re-entry. Therefore, the uncontrolled re-entry cases have a longer time to absorb the heat. Fig. 9 depicts the ground risk assessments. The predicted casualty area and kinetic energy on the ground are represented in Fig. 9(a) and (b), respectively. It can be seen that they increase in proportion to the size and mass of the cases.

Table 10 shows the details for the Monte Carlo simulations, where the final/initial mass ratio, casualty area, kinetic energy, and survivability percentage are presented

for the uncontrolled and controlled re-entries. Overall, both results are similar for each case. However, there are small differences in the mass ratio and kinetic energy for a few cases. The predicted survival masses from uncontrolled re-entry are lower due to the ablation, and consequently it leads to the lower kinetic energy. The results show that all the propellant tanks survived during re-entry, independently of their mass or size, since the considered material (which is taken to be a titanium alloy Ti-6Al-4V) has a high heat of fusion and melting temperature. Based on the results from Fig. 7, a change of the titanium material should be an effective design-for-demise technique. The casualty areas between 1 and 3.7 m^2 for a single propellant tank are obtained, and the kinetic energies at impact are always higher than 15 J. Therefore, the propellant tanks can pose a great risk to the people and properties on the ground, unless an alternative spacecraft design is used, involving the next generation of propellant tanks with an outer demisable shell and an internal thin liner of a harder demisable material, (Lips et al., 2017; Radtke, 2006).

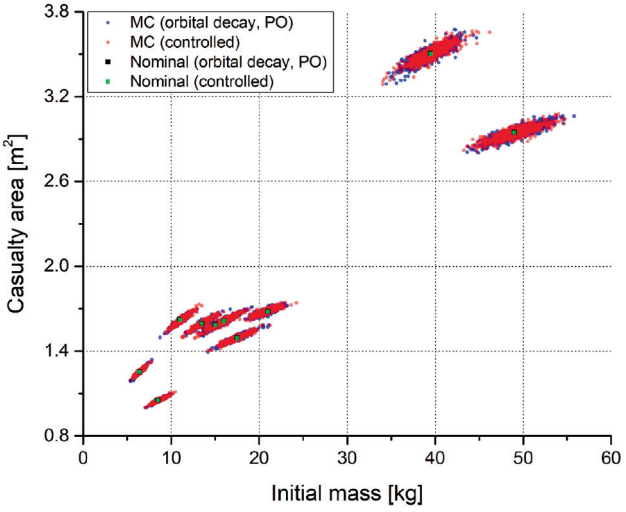

(a) Casualty area vs. initial mass

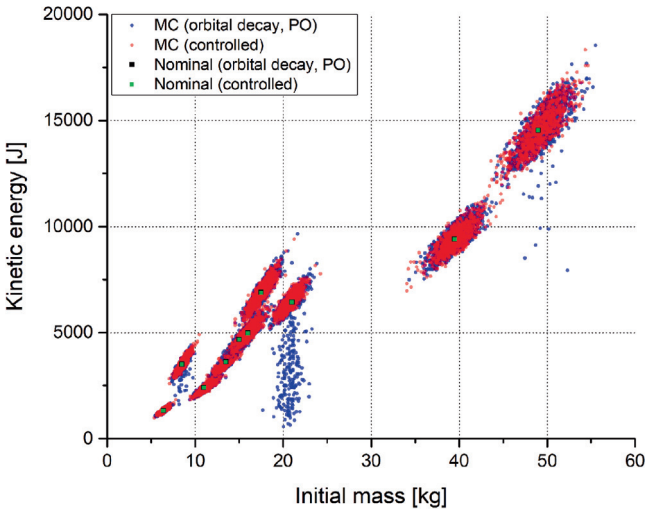

(b) Kinetic energy vs. initial mass

Fig. 9. Ground risk assessments for propellant tanks (cases 1 to 10).

4.3.2. Reaction wheels

Reaction wheels are commonly used in most spacecrafts and are known as a critical component in terms of re-entry casualty risk. For the uncertainty simulations, the reaction wheels were divided into three sub-components: the external housing, wheel, and motor. Modelling assumptions for reaction wheels are presented in Table 11.

The test cases were modelled based on Tables 2 and 3. In total, 18 different cases (12 cylinders and 6 boxes) were considered. The initial conditions used in Section 4.3.1 were used for the spacecraft analysis. The uncertainties in Table 8 were considered for the Monte Carlo simulations. The demise altitude and final/initial mass ratio are presented in Fig. 10(a) and (b), respectively. Overall, the demise altitudes from uncontrolled re-entry are higher than those from controlled re-entry. Fig. 11(a) and 11(b) show the casualty area and kinetic energy on the ground. The results from controlled re-entry are generally higher than those from uncontrolled re-entry because the cases from controlled re-entry are exposed to the atmosphere later as explained above. Thus, they induce a larger casualty area as well as a larger kinetic energy. More details are shown in Table 12. The demise altitude, casualty area, kinetic energy, and survivability rate are indicated for the uncontrolled and controlled re-entries. For the reaction wheel housing, all the cases (11, 14, 17, 20, 23, and 26), including the largest component, demised during re-entry. The material considered (AA7075), which has a low melting temperature and emissivity, is regarded as the main reason. Therefore, the reaction wheel housing is not considered a critical component in terms of ground risk casualty risk. The averaged demise altitudes were between 84.3 and 85.2 km in case of uncontrolled re-entry, but in the case of controlled re-entry, they were between 58.7 and 58.9 km due to its lower spacecraft break-up altitude. For each case, based on the averaged value, the minimum and maximum altitudes have a variability of around ±4 km.

For the flywheel, most cases demised for the uncontrolled re-entry cases, while most survived for the controlled re-entry ones. However, the flywheels cases numbers 15, 21, and 27 render a kinetic energy above 15 J for both re-entries. Among them, the case which has more than 50% survivability was only the case 21. Hence, the flywheels may not pose a great risk to the ground population. In the case of demise, the averaged demise altitudes were between 38.7 and 80.4 km depending on the spacecraft break-up altitude and the considered initial mass. The estimated casualty area were between 0.01 and 0.55 m^2. Although only three cases survived for the

Table 10
Monte Carlo simulations for propellant tanks.

Case	Mass Ratio (%)			Casualty Area (m^2)			Kinetic Energy (J)			Survivability (%)
	Avg.	Min	Max	Avg.	Min	Max	Avg.	Min	Max	Energy > 15 J
Uncontrolled Re-entry (PO)										
1	100	100	100	1.25	1.19	1.31	1330.5	1029.9	1668.6	100
2	99.5	70.0	100	1.05	1.00	1.09	3487.4	1593.1	4423.1	100
3	100	100	100	1.62	1.53	1.72	2411.2	1835.1	3024.0	100
4	100	100	100	1.59	1.50	1.69	3636.9	2914.5	4815.8	100
5	100	100	100	1.58	1.49	1.69	4694.1	3562.5	6234.8	100
6	100	100	100	1.61	1.51	1.69	5000.9	3710.8	6323.2	100
7	100	100	100	1.49	1.41	1.59	6916.2	5356.6	9661.3	100
8	92.9	31.9	100	1.68	1.60	1.76	5729.1	571.1	8252.9	100
9	100	100	100	3.50	3.34	3.66	9406.4	7489.1	11301.4	100
10	99.8	69.4	100	2.95	2.79	3.09	14547.1	7941.4	18551.5	100
Controlled Re-entry										
1	100	100	100	1.25	1.19	1.33	1334.0	982.5	1833.1	100
2	100	100	100	1.05	1.00	1.11	3531.6	2593.2	4905.4	100
3	100	100	100	1.62	1.53	1.73	2423.4	1826.6	3201.9	100
4	100	100	100	1.59	1.50	1.68	3623.0	2677.1	4483.2	100
5	100	100	100	1.59	1.49	1.68	4697.0	3534.8	6446.9	100
6	100	100	100	1.61	1.53	1.70	5004.3	3790.8	6317.0	100
7	100	100	100	1.49	1.41	1.58	6916.0	4805.3	9407.2	100
8	100	100	100	1.68	1.61	1.75	6475.0	5205.4	8165.4	100
9	100	100	100	3.51	3.29	3.66	9430.1	6970.8	12648.8	100
10	100	100	100	2.94	2.81	3.08	14597.4	11470.6	18343.8	100

Table 11
Physical properties of reaction wheels.

	Name	Shape	Width/Diameter (m)	Length (m)	Mass (kg)	Material
11	VRW-1 (housing)	Cylinder	0.115	0.077	0.30	AA7075
12	VRW-1 (wheel)	Cylinder	0.1035	0.0616	0.69	A316
13	VRW-1 (motor)	Box	0.0511	0.0511	0.81	A316
14	RSI68-170/60 (housing)	Cylinder	0.347	0.124	1.13	AA7075
15	RSI68-170/60 (wheel)	Cylinder	0.3123	0.0992	4.31	A316
16	RSI68-170/60 (motor)	Box	0.0873	0.0873	4.05	A316
17	RSI25-220/45 (housing)	Cylinder	0.347	0.124	1.19	AA7075
18	RSI25-220/45 (wheel)	Cylinder	0.3123	0.0992	2.11	A316
19	RSI25-220/45 (motor)	Box	0.0857	0.0857	3.90	A316
20	RW50 (housing)	Cylinder	0.25	0.12	0.76	AA7075
21	RW50 (wheel)	Cylinder	0.225	0.096	6.11	A316
22	RW50 (motor)	Box	0.0694	0.0694	2.43	A316
23	200SP-M (housing)	Cylinder	0.24	0.09	0.62	AA7075
24	200SP-M (wheel)	Cylinder	0.216	0.072	1.91	A316
25	200SP-M (motor)	Box	0.0833	0.0833	2.67	A316
26	HR16 (housing)	Cylinder	0.418	0.178	1.73	AA7075
27	HR16 (wheel)	Cylinder	0.3762	0.1424	4.37	A316
28	HR16 (motor)	Box	0.092	0.088	5.90	A316

uncontrolled re-entry cases, twelve cases survived for the controlled re-entry ones. It can be noted that the cases from controlled re-entry have higher survivability, and consequently it can lead to higher ground risk. A caution is thus needed when the spacecraft demise from controlled re-entry reaches the populated area.

For the reaction wheel motor, only case 28 survived for the uncontrolled re-entry whereas most of the cases demised for the controlled re-entry. For the demised cases, the averaged demise altitudes were between 38.0 and 69.8 km. For the survived ones, the casualty area were between 0.08 and 0.45 km. From the Monte Carlo simulations in the surviving cases, the combination of low exposure altitudes, low atmospheric densities, high values of certain material properties (emissivity and melting temperature) and low aerothermodynamics was considered as the main factors for the survivability. Therefore, either a change of the material, an early exposure, and/or a mass/-size reduction could lead to the reaction wheel motor demise.

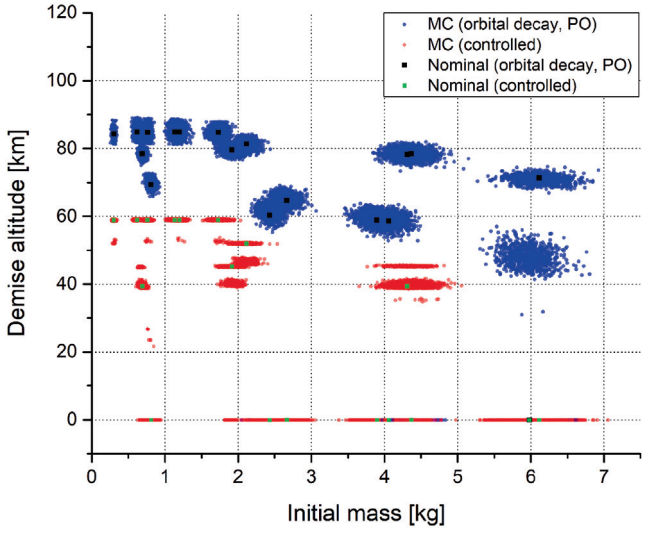

(a) Demise altitude vs. initial mass

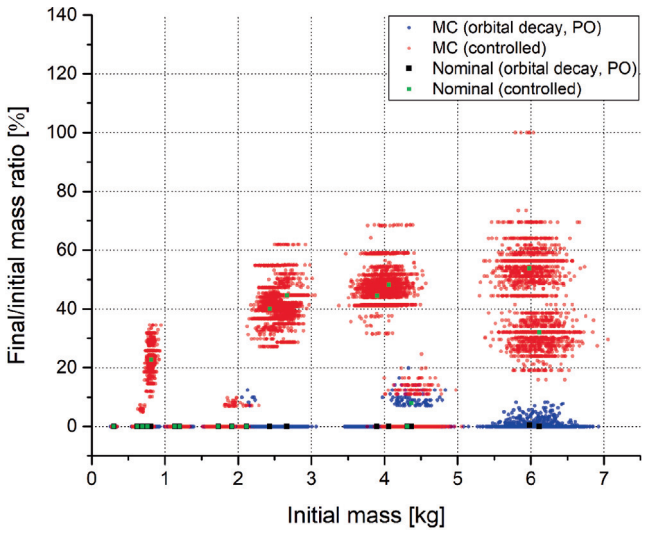

(b) Final/initial mass ratio vs. initial mass

Fig. 10. Survivability results for reaction wheels (cases 11 to 28).

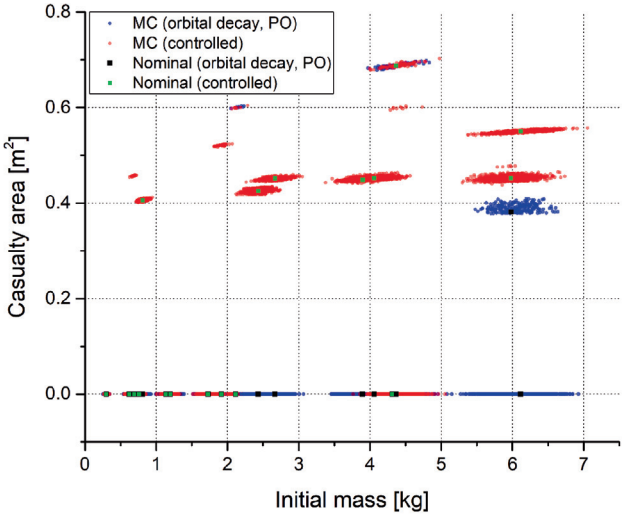

(a) Casualty area vs. initial mass

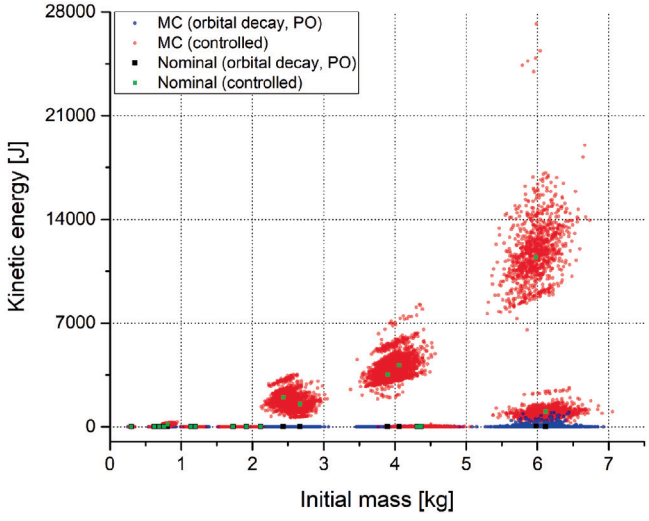

(b) Kinetic energy vs. initial mass

Fig. 11. Ground risk assessments for reaction wheels (cases 11 to 28).

4.3.3. Magnetic torquers

The magnetic torquers are also common spacecraft components and are known as a critical component for the re-entry casualty risk due to their late exposure to the atmosphere. For the analyses, the magnetic torquers were divided into three sub-components: the external housing, wiring, and core. It was assumed that these components are exposed to the atmosphere sequentially, i.e. the wiring starts to be ablated once the external housing has demised. Modelling assumptions for magnetic torquers are presented in Table 13.

In total, 18 different cylinder cases were considered. The initial conditions and uncertainties presented in Section 4.3.1 were used. Fig. 12 shows the re-entry survivability results for cases 29 to 46. The demise altitudes and the ratio of the final mass to the initial mass are presented in Fig. 12(a) and (b), respectively. Again, it can be noted that the demise altitudes from uncontrolled re-entry are generally higher than those from controlled re-entry due to their early exposure to the atmosphere from spacecraft break-up. Hence, there are more survived cases without ablation from controlled re-entry than those from uncontrolled re-entry. Casualty area and kinetic energy are also generally larger than those from uncontrolled re-entry as can be seen in Fig. 13. Although case 43 (MT400-2) from uncontrolled re-entry has the maximum kinetic energy, relatively high survived masses from controlled re-entry lead to a larger casualty area as well as higher kinetic energy.

Table 12
Monte Carlo simulations for reaction wheels.

Case	Demise Altitude (km)			Casualty Area (m^2)			Kinetic Energy (J)			Survivability (%)
	Avg.	Min	Max	Avg.	Min	Max	Avg.	Min	Max	Energy > 15 J
Uncontrolled Re-entry (PO)										
11	84.3	81.3	88.4	0	0	0	0	0	0	0
12	78.6	75.1	82.2	0	0	0	0	0	0	0
13	69.8	65.9	72.8	0	0	0	0	0	0	0
14	85.1	81.2	88.7	0	0	0	0	0	0	0
15	78.2	74.9	81.5	0	0	0	0	0	0	0
16	59.2	52.8	63.8	0	0	0	0	0	0	0
17	84.8	81.5	88.6	0	0	0	0	0	0	0
18	80.4	0	84.3	0.01	0	0.60	0.05	0	9.62	0
19	59.2	52.8	63.4	0	0	0	0	0	0	0
20	84.6	81.6	88.9	0	0	0	0	0	0	0
21	71.0	67.0	74.7	0	0	0	0	0	0	0
22	61.1	55.4	65.7	0	0	0	0	0	0	0
23	85.2	81.8	89.1	0	0	0	0	0	0	0
24	79.7	76.6	82.6	0	0	0	0	0	0	0
25	65.1	60.6	69.2	0	0	0	0	0	0	0
26	84.8	81.5	87.9	0	0	0	0	0	0	0
27	72.0	0	82.0	0.06	0	0.70	1.47	0	69.39	4.0
28	38.0	0	57.0	0.08	0	0.41	36.48	0	968.8	17.7
Controlled Re-entry										
11	58.7	51.9	59.2	0	0	0	0	0	0	0
12	38.8	0	45.3	0.01	0	0.46	0.04	0	2.85	0
13	0.15	0	26.8	0.40	0	0.41	150.5	0	329.7	99.3
14	58.9	58.7	59.3	0	0	0	0	0	0	0
15	38.8	0	40.1	0.01	0	0.60	0.80	0	174.6	1.0
16	0	0	0	0.45	0.44	0.46	4110.0	1883.5	8281.1	100
17	58.9	52.5	59.2	0	0	0	0	0	0	0
18	49.2	0	52.3	0.01	0	0.60	0.03	0	4.07	0
19	0	0	0	0.45	0.44	0.46	3859.2	2000.3	8067.4	100
20	58.9	52.5	59.2	0	0	0	0	0	0	0
21	0	0	0	0.55	0.54	0.56	986.1	253.7	2643.9	100
22	0	0	0	0.43	0.42	0.43	2025.7	1006.2	3526.7	100
23	58.9	58.7	59.3	0	0	0	0	0	0	0
24	42.4	0	45.5	0.02	0	0.52	0.24	0	12.10	0
25	0	0	0	0.45	0.44	0.46	1419.7	630.1	3077.3	100
26	58.8	52.1	59.2	0	0	0	0	0	0	0
27	38.7	0	45.7	0.07	0	0.70	3.07	0	76.83	9.5
28	0	0	0	0.45	0.44	0.48	11836.6	6552.3	27199.7	100

More details are shown in Table 14. The demise altitude, casualty area, kinetic energy, and survivability percentage are presented. The magnetic torquer housings represent cases 29, 32, 35, 38, 41, and 44, and all of them demised during re-entry due to the low melting temperature and emissivity of the considered material (AA7075). The magnetic torquer housing is hence not considered a critical component along with the reaction wheel housing. The averaged demise altitudes were between 79.9 and 84.4 km, and 39.2 and 58.9 km for the uncontrolled and controlled re-entries, respectively. All the magnetic torquer wirings (cases 30, 33, 36, 39, 42, and 45) were also demised regardless of their size or mass in case of uncontrolled re-entry. However, cases 36, 39, 42, and 45 survived in case of controlled re-entry, and they even had more than 50% survivability. The controlled re-entry corresponds to lower demise altitudes of the spacecraft as well as external housing, and consequently the lower demise altitudes lead to a later exposure of the internal elements (wirings) to the aerodynamic heating.

For the magnetic torquer core, all the cases survived for the controlled re-entry, but for the uncontrolled re-entry, cases 31, 34, and 40 demised. It can be noted that the magnetic torquer cores have a higher survivability than the housings and wirings because they are the innermost components from sequential ablation process (inner components are exposed to the atmosphere after the external components demise). Therefore, the magnetic torquer core can pose a risk to the ground population. For the survived cases, the averaged casualty area and kinetic energy were between 0.002 and 0.57 m^2, and 0.32 and 6643.3 J, respectively.

Table 13
Physical properties of magnetic torquers.

Case	Name	Shape	Diameter (m)	Length (m)	Mass (kg)	Material
29	MT15-1 (housing)	Cylinder	0.0167	0.3295	0.09	AA7075
30	MT15-1 (wiring)	Cylinder	0.0126	0.3295	0.17	Copper
31	MT15-1 (core)	Cylinder	0.0092	0.3295	0.17	Iron
32	MT30-2 (housing)	Cylinder	0.0271	0.4045	0.28	AA7075
33	MT30-2 (wiring)	Cylinder	0.0205	0.4045	0.56	Copper
34	MT30-2 (core)	Cylinder	0.015	0.4045	0.56	Iron
35	MT80-1 (housing)	Cylinder	0.0478	0.3805	0.82	AA7075
36	MT80-1 (wiring)	Cylinder	0.0362	0.3805	1.64	Copper
37	MT80-1 (core)	Cylinder	0.0264	0.3805	1.64	Iron
38	MT140-2 (housing)	Cylinder	0.0407	0.68	1.06	AA7075
39	MT140-2 (wiring)	Cylinder	0.0308	0.68	2.12	Copper
40	MT140-2 (core)	Cylinder	0.0225	0.68	2.12	Iron
41	MT400-2 (housing)	Cylinder	0.0558	0.75	2.20	AA7075
42	MT400-2 (wiring)	Cylinder	0.0422	0.75	4.40	Copper
43	MT400-2 (core)	Cylinder	0.0308	0.75	4.40	Iron
44	MT400-2-L (housing)	Cylinder	0.0417	0.952	1.56	AA7075
45	MT400-2-L (wiring)	Cylinder	0.0316	0.952	3.12	Copper
46	MT400-2-L (core)	Cylinder	0.023	0.952	3.12	Iron

4.3.4. Balance masses and payload components

The balance masses are likely to survive during re-entry since they correspond to heavy blocks of materials than present high resistance to heat. The payload components are different for each spacecraft depending on the mission scenarios. However, there are some common types of payload for typical reference missions. Some of the components such as telescopes, lenses, or mirrors may partially survive during re-entry; therefore, they can be considered as critical components in terms of re-entry risk. A model of a telescope and a star tracker were considered for the payload components. The telescope was divided into three sub-components: the telescope tube, mirror, and optical box housing. The star tracker was divided into four sub-components: The baffle, box housing, optical caging, and optical lens. Modelling assumptions for balance masses and payload components are presented in Table 15. The aluminium alloy (AA7075), stainless steel (A316), reinforced carbon–carbon (RCC), zerodur, silicon carbide (SiC), titanium alloy (Ti6 Al-4V), and glass were used as materials.

The payload components were modelled based on the values given in Table 5. In total, 10 different test cases (5 cylinders and 5 boxes) were considered. The initial conditions and uncertainties presented in Section 4.3.1 were used. Fig. 14 shows the re-entry survivability results. The demise altitude and final/initial mass ratio are shown in Fig. 14(a) and (b), respectively. It can be noted that cases 51, 53, 55, and 56 of payload components demised for the uncontrolled and controlled re-entries. However, cases 48 and 49 of balance masses are partially demised. They demised for the uncontrolled re-entry while survived for the controlled re-entry. The survived masses of test cases from controlled re-entry are generally higher than that from uncontrolled re-entry due to their late exposure to the atmosphere. The cases from uncontrolled re-entry have enough time to be ablated relatively. The predicted casualty area and kinetic energy on the ground are represented in Fig. 15(a) and (b), respectively. Cases 50 and 52 (telescope tube and optical box housing) render a high casualty area, and case 47 (Sentinel-1) has the highest kinetic energy due to its high mass. More details are presented in Table 16.

For the balance masses (cases 47 to 49), small masses (less than 20 kg) were almost demised during re-entry from the uncontrolled re-entry, but heavy balance masses (more than 20 kg) survived with 100% survivability rate (energy $>$ 15 J). The averaged demise altitudes were 49.1 and 60.4 km for cases 48 and 49, respectively. On the other hand, all the balance masses survived from the controlled re-entry. Based on the Monte Carlo simulations, the material properties and spacecraft break-up altitude were regarded as the main factors for the survivability. Therefore, either a change of the material, an early exposure, and/or a mass/-size reduction can lead to the balance mass demise. The maximum averaged casualty area was estimated to be 0.6 m^2 for the survived cases with high kinetic energy. Thus, the balance masses may pose a risk to the properties and ground population. Design of balance masses hence require caution in this sense. For the payload components (cases 50 to 56), the cases 50 and 52 always survived during re-entry since they are made of reinforced carbon–carbon and silicon carbide which have high thermal properties (melting temperature and emissivity). Therefore, they survived without ablation during re-entry. Case 54 concerns the use of a titanium alloy, and this case also survived due to its high melting temperature and heat of ablation. However, it was partially ablated or demised when considering the uncertainty analyses. Hence, this analysis gives that reinforced carbon–carbon and silicon carbide are materials that are more hard to be ablated in these cases. All the other cases (51, 53, 55, and 56) demised during

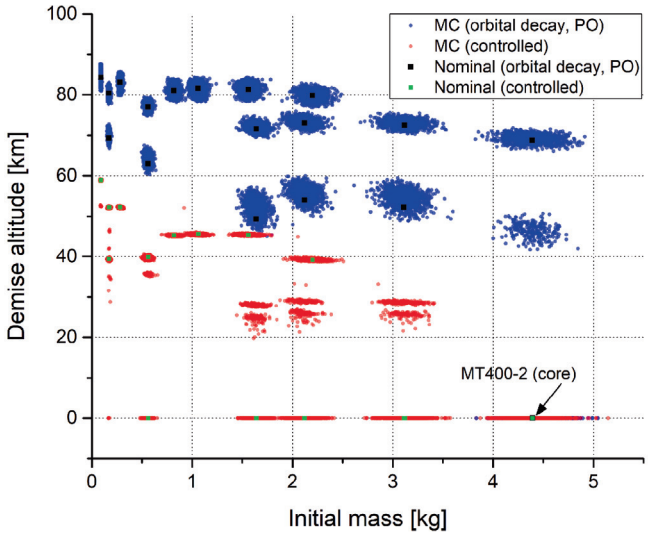

(a) Demise altitude vs. initial mass

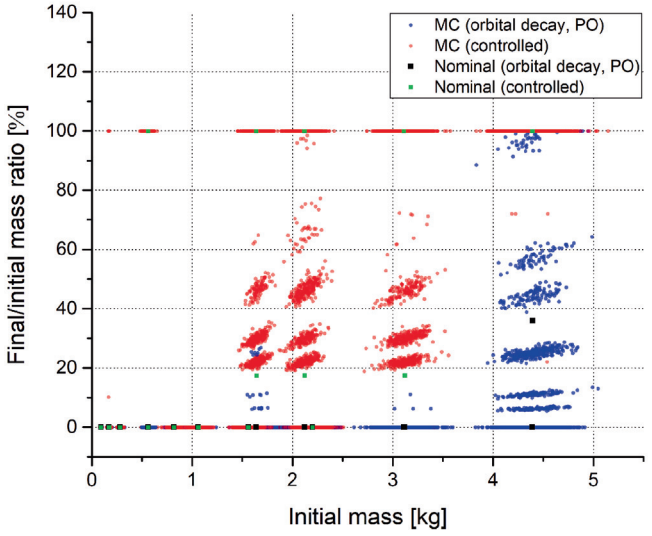

(b) Final/initial mass ratio vs. initial mass

Fig. 12. Survivability results for magnetic torquers (cases 29 to 46).

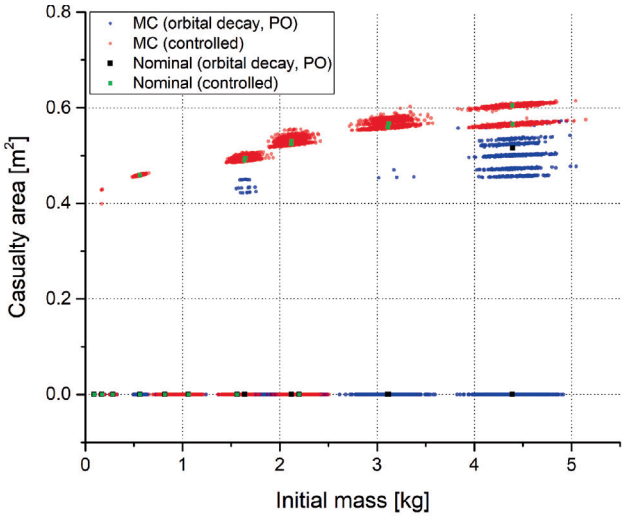

(a) Casualty area vs. initial mass

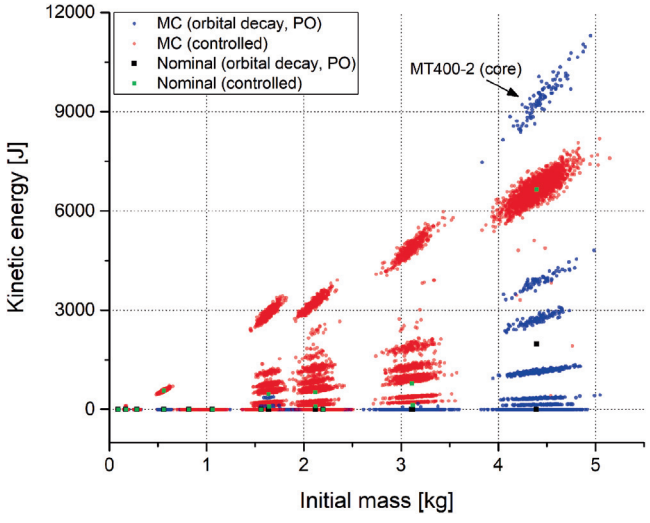

(b) Kinetic energy vs. initial mass

Fig. 13. Ground risk assessments for magnetic torquers (cases 29 to 46).

re-entry. The survived cases had casualty areas between 2.51 and 2.99 m^2 with high kinetic energy. Therefore, some payload components such as telescope tubes and box housings can pose a great risk to ground population.

5. Conclusions

Re-entry analysis of critical components of a spacecraft has been conducted. The objective of this work was to gain an understanding for the effects of uncertainties on the re-entry analysis in terms of re-entry casualty risk, by providing a qualitative simulations. Particular attention was focused on the re-entry survivability of the current critical components identified after the spacecraft break-up. The analysis was divided into two main phases: (1) re-entry simulation of spacecraft debris from an initial condition to thermal break-up and (2) re-entry survivability assessment of critical components after the break-up. In the simulations, the uncertainties were estimated using Monte Carlo simulations and the results were compared with the nominal results (without uncertainties).

Regarding the spacecraft break-up, two different uncontrolled (Polar Orbit) and controlled re-entry scenarios were mainly used as the initial conditions. For the break-up mechanism, ablation (melting) was considered using the parent and child relationship. The results have shown that the break-up altitudes of uncontrolled re-entry are higher than those of controlled re-entry since the trajectories from Polar orbit maintain a relatively higher altitude for a long

Table 14
Monte Carlo simulations for magnetic torquers.

Case	Demise Altitude (km)			Casualty Area (m^2)			Kinetic Energy (J)			Survivability (%)
	Avg.	Min	Max	Avg.	Min	Max	Avg.	Min	Max	Energy > 15 J
Uncontrolled Re-entry (PO)										
29	84.4	81.0	87.7	0	0	0	0	0	0	0
30	80.5	77.8	83.1	0	0	0	0	0	0	0
31	70.2	66.8	72.8	0	0	0	0	0	0	0
32	83.1	79.9	85.8	0	0	0	0	0	0	0
33	77.4	74.9	79.5	0	0	0	0	0	0	0
34	64.2	60.3	67.6	0	0	0	0	0	0	0
35	81.2	78.2	84.2	0	0	0	0	0	0	0
36	72.0	69.4	74.8	0	0	0	0	0	0	0
37	51.0	0	57.1	0.01	0	0.45	3.54	0	375.9	2.1
38	81.5	78.4	84.4	0	0	0	0	0	0	0
39	73.3	70.5	76.1	0	0	0	0	0	0	0
40	55.6	47.9	60.0	0	0	0	0	0	0	0
41	79.9	77.0	82.9	0	0	0	0	0	0	0
42	69.2	66.1	71.9	0	0	0	0	0	0	0
43	11.1	0	50.7	0.38	0	0.57	1798.5	0	11302.1	76
44	81.4	78.5	84.4	0	0	0	0	0	0	0
45	72.9	70.3	75.7	0	0	0	0	0	0	0
46	54.3	0	59.5	0.002	0	0.47	0.42	0	175.0	0.4
Controlled Re-entry										
29	58.9	52.4	59.2	0	0	0	0	0	0	0
30	52.1	41.9	52.5	0	0	0	0	0	0	0
31	39.1	0	39.9	0.002	0	0.43	0.32	0	109.2	0.3
32	52.2	51.8	52.6	0	0	0	0	0	0	0
33	39.4	35.0	40.6	0	0	0	0	0	0	0
34	0	0	0	0.46	0.45	0.46	568.6	449.8	727.1	100
35	45.2	44.9	45.6	0	0	0	0	0	0	0
36	12.4	0	28.6	0.27	0	0.51	127.3	0	919.3	54.1
37	0	0	0	0.49	0.49	0.50	1733.6	483.5	3438.9	100
38	45.5	45.1	52.0	0	0	0	0	0	0	0
39	9.28	0	33.2	0.36	0	0.56	264.9	0	2577.2	66.4
40	0	0	0	0.52	0.52	0.53	1732.8	555.1	3912.8	100
41	39.2	38.7	44.9	0	0	0	0	0	0	0
42	0	0	0	0.61	0.58	0.62	6634.8	405.3	8186.2	100
43	0	0	0	0.57	0.56	0.58	6643.3	1925.6	7799.4	100
44	45.4	45.0	45.9	0	0	0	0	0	0	0
45	9.81	0	33.2	0.37	0	0.60	299.5	0	3909.5	64.5
46	0	0	0	0.56	0.55	0.57	2599.6	847.2	5981.6	100

Table 15
Physical properties of balance masses and payload components.

Case	Name	Shape	Width/Diameter (m)	Length (m)	Mass (kg)	Material
			Balance mass			
47	Sentinel-1 (internal)	Box	0.184	0.184	50.0	A316
48	Sentinel-1 (external)	Box	0.082	0.082	4.50	A316
49	Sentinel-5P	Box	0.175	0.175	15.0	AA7075
			Payload (Telescope)			
50	Telescope tube	Cylinder	0.65	1.80	59.7	RCC
51	Primary mirror	Cylinder	0.65	0.03	22.6	Zerodur
52	Optical box housing	Box	1.15	0.70	15.8	SiC
			Payload (Star tracker)			
53	Baffle	Cylinder	0.054	0.14	0.17	AA7075
54	Box housing	Box	0.120	0.12	1.13	Ti-6Al-4 V
55	Optical caging	Cylinder	0.048	0.05	0.07	Ti-6Al-4 V
56	Optical lens	Cylinder	0.048	0.02	0.09	Glass

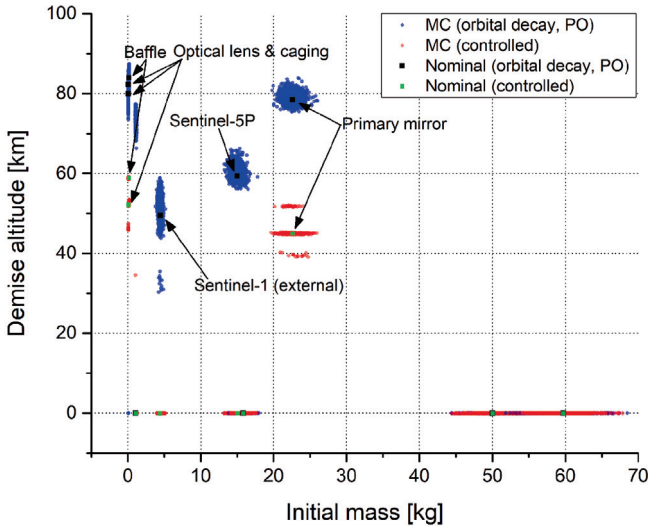

(a) Demise altitude vs. initial mass

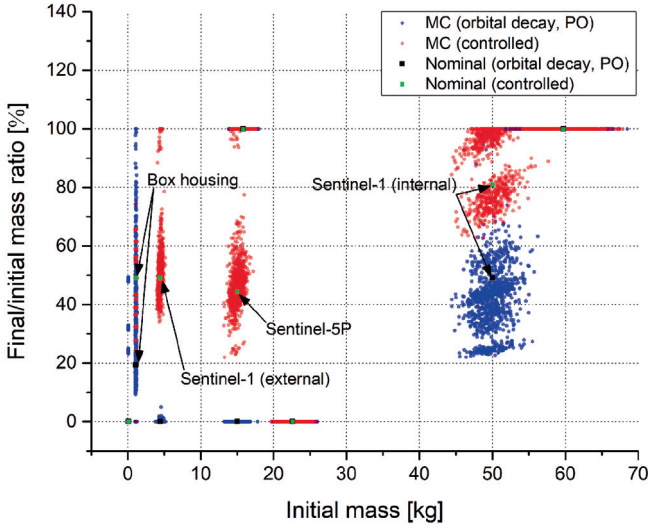

(b) Final/initial mass ratio vs. initial mass

Fig. 14. Survivability results for balance masses and payloads (cases 47 to 56).

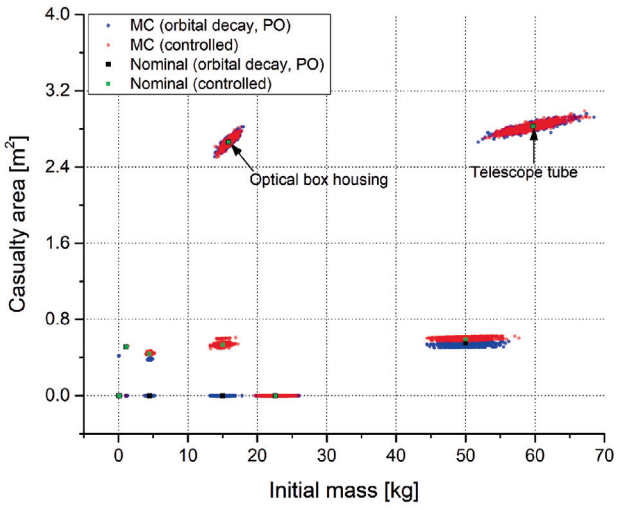

(a) Casualty area vs. initial mass

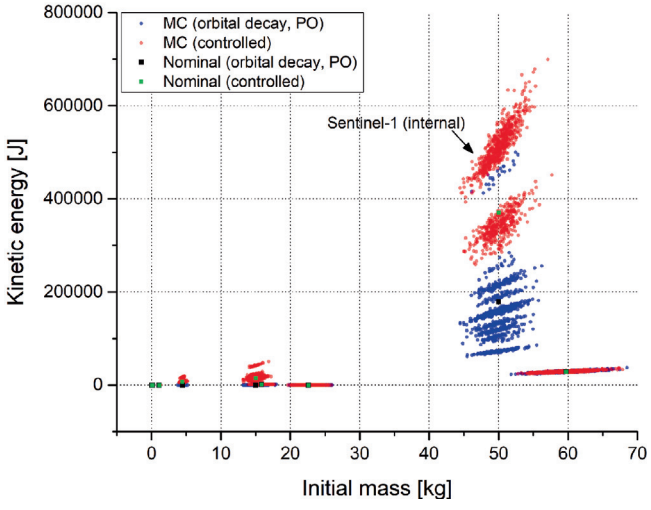

(b) Kinetic energy vs. initial mass

Fig. 15. Ground risk assessments for balance masses and payloads (cases 47 to 56).

time before re-entry into the atmosphere due to the shallow flight path angle. To investigate the effects of uncertainties, the sensitivity analysis was performed using Monte Carlo simulations. A total of 6 categories, which are the initial condition, atmosphere, size, aerodynamics, aerothermodynamics, and material properties were considered. It is found that the material properties are the most dominant uncertainty parameters in the break-up altitude prediction. The initial conditions, size, and aerodynamic factors are also noticeable.

Concerning the re-entry survivability and ground risk assessment of critical components, the propellant tanks, reaction wheels, balance masses, magnetic torquers, and payloads were used as the test models. The test cases were modelled based on vendor supplied information and reverse engineering, and, in total, 56 cases were considered. In the simulations, the most critical components were the propellant tank and some balance masses and payload components (telescope tube and optical box housing), since they are usually made of materials such as reinforced carbon–carbon or titanium alloys which have high thermal resistance properties (melting temperature and heat of fusion). The magnetic torquer core which is well protected within the magnetic torquer housing and the corresponding wires also had a high survivability due to their late exposure to the atmosphere. The study shows that they could pose a great risk to people and properties on the ground, unless an alternative design is used. For the reaction wheels

Table 16
Monte Carlo simulations for balance masses and payloads.

Case	Demise Altitude (km)			Casualty Area (m^2)			Kinetic Energy (J)			Survivability (%)
	Avg.	Min	Max	Avg.	Min	Max	Avg.	Min	Max	Energy > 15 J
Uncontrolled Re-entry (PO)										
47	0	0	0	0.54	0.50	0.62	155072.5	61886.8	500322.0	100
48	49.1	0	58.9	0.02	0	0.39	1.09	0	313.1	1.8
49	60.4	56.1	66.3	0	0	0	0	0	0	0
50	0	0	0	2.83	2.66	2.96	29108.1	23198.4	37648.7	100
51	79.1	75.6	83.9	0	0	0	0	0	0	0
52	0	0	0	2.66	2.51	2.82	1336.0	1023.2	1638.2	100
53	83.7	80.8	87.5	0	0	0	0	0	0	0
54	32.4	0	77.4	0.29	0	0.52	48.23	0	541.5	43.7
55	65.7	0	84.5	0.08	0	0.42	0.31	0	5.14	0
56	82.9	79.7	86.1	0	0	0	0	0	0	0
Controlled Re-entry										
47	0	0	0	0.60	0.57	0.62	447757.6	259601.0	699559.0	100
48	0	0	0	0.44	0.43	0.47	7445.6	4389.8	19165.8	100
49	0	0	0	0.54	0.49	0.61	16565.9	5937.6	50916.2	100
50	0	0	0	2.83	2.70	2.99	29159.3	24093.8	36759.3	100
51	45.1	39.1	52.1	0	0	0	0	0	0	0
52	0	0	0	2.66	2.51	2.82	1329.5	1096.9	1656.8	100
53	55.6	52.0	59.2	0	0	0	0	0	0	0
54	0.02	0	34.6	0.51	0	0.52	114.1	0	284.9	99.9
55	52.0	45.9	52.4	0	0	0	0	0	0	0
56	56.5	51.8	59.1	0	0	0	0	0	0	0

and magnetic torquers, most of cases demised during re-entry due to the materials considered for their construction. However, some cases with large masses were partially ablated or survived. It can be noted that either a change of the material, an early exposure, and/or a mass/size reduction can lead to the components demise.

Furthermore, for the two different re-entry scenarios, the results have shown that the cases from controlled re-entry have a higher survivability due to their late exposure to the atmosphere, and consequently lead to a higher ground risk. Hence, particular caution is needed when the demising spacecraft from controlled re-entry reaches populated areas. The next step in this research stream is the identification of design-for-demise techniques for both system and sub-system levels to reduce overall casualty risk.

The sensitivity study of demise of critical components of spacecraft to uncertainties were treated here by Monte-Carlo simulations. In future works more elaborate schemes could be envisaged, taking into account notably the skewness of the statistical distributions that are induced by the ongoing trajectory heating and the trajectory attitude of the components. This is indeed a topic of recent research and interest to the analysis of space debris demise.

Declaration of Competing Interest

The authors declare that they have no known competing financial interests or personal relationships that could have appeared to influence the work reported in this paper.

Acknowledgements

This work was supported by a Swiss Government Excellence Scholarship (ESKAS No. 2019.0535) awarded by Federal Commission for Scholarships (FCS). An initial version of part of this work was partially supported by the European Space Agency project (ESA Contract No. 4000112200/14/NL/GLC) under a Deimos Space subcontract. The authors thank Christian Kanesan and Gwenael Hannema for their contributions to this work.

Appendix A.

Materials	Material properties					
	ρ (kg/m^3)	T_{melt} (K)	h_f (kJ/kg)	C_p (J/kg-K)	k (W/m-K)	ε (-)
AA7075	2801	870	385	746.4	130	0.15
A316	8030	1650	274	611.5	19	0.59
Ti-6Al-4V	4437	1900	400	746.4	6.7	0.39
Copper	8960	1356	243	434.1	385	0.26
Iron	7865	1812	272	711.5	76.2	0.59
Reinforced Carbon–Carbon	1688.5	2144	37.7	785.1	110	0.9
Zerodur	2530	1424	250	842.4	1.64	0.9
Silicon Carbide	3200	3103	370	672	77.5	0.9
Glass	2500	923	232	800	1.1	0.89

References

Anderson, J.D., 2006. Hypersonic and high temperature gas dynamics, second ed. AIAA Education Series.

Barka, L., Balat-pichelin, M., Annaloro, J., Omaly, P., 2006. 'Influence of oxidation and emissivity for metallic alloys space debris during their atmospheric entry'. In: 7th European Conference on Space Debris, Darmstadt, Germany.

Blue Canyon Technologies, 2020. 'Reaction wheels [Online], Accessed August, 2020'. URL https://bluecanyontech.com/components

Carnà, S.F.R., Bevilacqua, R., 2019. High fidelity model for the atmospheric re-entry of cubesats equipped with the drag de-orbit device. Acta Astronaut. 156, 134–156.

Collins Aerospace, 2020. 'Space wheels [Online], Accessed August, 2020'. URL https://www.collinsaerospace.com/what-we-do/Space/Space-Wheels

Cropp, L.O., 1965. 'Analytical methods used in predicting the re-entry ablation of spherical and cylindrical bodies', Sandia Corporation SC-RR-65-187.

EADS Astrium GmbH, 2015. 'Spacecraft propellant tank manufacture [Online], Accessed August, 2019'. URL http://cs.astrium.eads.net/sp/spacecraft-propulsion/propellant-tanks/manufacturing.html

Fuentes, I.P., Bonetti, D., Letterio, F., de Miguel, G.V., Arnao, G.B., Palomo, P., Parigini, C., Lemmens, S., Lips, T., Kanzler, R., 2019. Upgrade of esa's debris risk assessment and mitigation analysis (drama) tool: spacecraft entry survival analysis module. Acta Astronaut. 158, 148–160.

Goulard, R., 1958. On catalytic recombination rates in hypersonic stagnation heat transfer. J. Jet Propul. 28 (11), 737–745.

Haslehurst, A., Lewis, S., 2011. The use of dry lubricated bearings in reaction wheels. In: Proceedings of the 14th European Space Mechanisms and Tribology Symposium–ESMATS 2011, pp. 253–261.

Honeywell Aerospace Electronic Systems, 2020. 'Constellation series reaction wheels [Online], Accessed August, 2020'. URL ftp://apollo.ssl.berkeley.edu/pub/Pointing_Studies/Hardware/Honeywell%20Reaction%20Wheels.pdf.

Kärräng, P., Lips, T., Soares, T., 2019. Demisability of critical spacecraft components during atmospheric re-entry. J. Space Safety Eng. 6 (3), 181–187.

Kato, A., 2001. Comparison of national space debris mitigation standards. Adv. Space Res. 28 (9), 1447–1456.

Kelley, R.L., Rochelle, W.C., 2012. 'Atmospheric reentry of a hydrazine tank', NASA White paper, Houston, TX. pp. 1–11.

Klett, R.D., 1964. 'Drag coefficients and heating ratios for right circular cylinders in free-molecular and continuum flow from mach 10 to 30', Sandia Corporation SC-RR-64-2141.

Klinkrad, H., 2010. Space debris - models and risk analysis. Springer-Verlag, Berlin Heidelberg.

Klinkrad, H., Bohlmann, U.M., 2008. 'Requirements on space debris mitigation for esa projects'. In: Presentation to the 48th session of the Legal Subcommitte of the UN Committee on the Peaceful Uses of Outer Space. URL https://www.unoosa.org/pdf/pres/lsc2009/pres-07.pdf

Liou, J.-C., Opiela, J.N., Vavrin, A.B., Draegar, B., Anz-Meador, P.D., Ostrom, C.L., Sanchez, C., 2015. 'Debris assessment software user's guide: Version 3.0 [Online], Accessed August, 2019'. URL https://orbitaldebris.jsc.nasa.gov/

Lips, T., Fritsche, B., 2005. A comparison of commonly used re-entry analysis tools. Acta Astronaut. 57 (2–8), 312–323.

Lips, T., Fritsche, B., Kanzler, R., Schleutker, T., Gülhan, A., Bonvoisin, B., Soares, T., Sinnema, G., 2017. About the demisability of propellant tanks during atmospheric re-entry from leo. J. Space Safety Eng. 4 (2), 99–104, https://www.sciencedirect.com/science/article/pii/S2468896717300484.

L.L.C. MatWeb (2015), 'Matweb-material property data [Online], Accessed August, 2019'. http://www.matweb.com/.

Mehta, P.M., Kubicek, M., Minisci, E., Vasile, M., 2017. Sensitivity analysis and probabilistic re-entry modeling for debris using high dimensional model representation based uncertainty treatment. Adv. Space Res. 59 (1), 193–211.

O'Connor, B., 2008. 'Handbook for limiting orbital debris', Tech. Rep. NASA Handbook 8719.14, National Aeronautics and Space Administration, Washington, DC 20546.

Park, S.-H., Kim, H.-D., Park, G., 2018. Orbit, orbital lifetime, and reentry survivability estimation for orbiting objects. Adv. Space Res. 62 (11), 3012–3032.

Park, S.-H., Kim, J., Choi, I., Park, G., 2021. Experimental study of separation behavior of two bodies in hypersonic flow. Acta Astronaut. 181, 414–426.

Park, S.-H., Laboulais, J.N., Leyland, P., Mischler, S., 2021. Re-entry survival analysis and ground risk assessment of space debris considering by-products generation. Acta Astronaut. 179, 604–618.

Park, S.-H., Park, G., 2017. Reentry trajectory and survivability estimation of small space debris with catalytic recombination. Adv. Space Res. 60 (5), 893–906.

Park, S.-H., Park, G., 2018. 'Separation process of spheres in hypersonic flows'. In: 2018 AIAA Atmospheric Flight Mechanics Conference, Kissimmee, Florida, AIAA-2018-0288.

Park, S.-H., Park, G., 2019. Separation process of multi-spheres in hypersonic flow. Adv. Space Res. 65 (1), 392–406.

Radtke, W., 2004. Manufacturing of advanced titanium (lined) propellant tanks and high pressure vessels. In: 4th International Spacecraft Propulsion Conference ESA-SP-555.

Radtke, W., 2005. Manufacturing and testing of advanced over-wrapped propellant tanks and high pressure vessels. In: 5th International Spacecraft Propulsion Conference ESA publications.

Radtke, W., n.d. 'Novel manufacturing methods for titanium tanks and liners'. In: 42nd AIAA/ASME/SAE/ASEE Joint Propulsion Conference & Exhibit AIAA-2006-5269.

Riley, D., Fuentes, I.P., Parigini, C., Meyer, J.-C., Leyland, P., Hannema, G., Guzman, E., Kanesan, C., Lips, T., 2015. '"design for demise" techniques to reduce re-entry casualty risk'. In: 66th International Astronautical Congress, Jerusalem, Israel pp. 1–9.

Rochelle, W.C., Kinsey, R.E., Reid, E.A., Reynolds, R.C., Johnson, N.L., 1997. 'Spacecraft orbital debris reentry aerothermal analysis'. In: Proceeding of the 8th Annual Thermal and Fluids Analysis Workshop Spacecraft Analysis and Design.

San-Juan, J.F., Pérez, I., San-Martín, M., Vergara, E.P., 2017. Hybrid sgp4 orbit propagator. Acta Astronaut. 137, 254–260.

Sanson, F., Bertorello, C., Bouilly, J.-M., Congedo, P.M., 2019. Breakup prediction under uncertainty: Application to upper stage controlled reentries from gto orbit. Aerosp. Sci. Technol. 87, 340–356.

Sato, T., 1999. Shape estimation of space debris using single-range doppler interferometry. IEEE Trans. Geosci. Remote Sens. 37 (2), 1000–1005.

Schmidt, U., Kühl, C., Michel, K., 2006. Advanced star sensors based on active pixel sensor technology. In: 6th International ESA Conference on Guidance, Navigation and Control Systems, Greece, ESA, p. SP-606..

Sim, H.S., Kim, K.H., 2011. Reentry survival analysis of tumbling metallic hollow cylinder. Adv. Space Res. 48 (5), 914–922.

Trisolini, M., Lewis, H.G., Colombo, C., 2018a. Demisability and survivability sensitivity to design-for-demise techniques. Acta Astronaut. 145, 357–384.

Trisolini, M., Lewis, H.G., Colombo, C., 2018b. Spacecraft design optimisation for demise and survivability. Aerosp. Sci. Technol. 77, 638–657.

VECTRONIC Aerospace GmbH, 2020. 'VRW Reaction wheels [Online], Accessed August, 2020'. URL https://www.vectronic-aerospace.com/reaction-wheels/.

Waswa, P.M.B., Elliot, M., Hoffman, J.A., 2013. Spacecraft design-for-demise implementation strategy and decision-making methodology for low earth orbit missions. Int. J. Des. Eng. 51 (9), 1627–1637.

Waswa, P.M.B., Hoffman, J.A., 2012. Illustrative nasa low earth orbit spacecraft subsystems design-for-demise trade-offs, analyses and limitations. Int. J. Des. Eng. 5 (1), 21–40.

Weiland, C., 2010. Computational space flight mechanics. Springer.

Wu, Z.N., Hu, R.F., Qu, X., Wang, X., Wu, Z., 2011. Space debris reentry analysis methods and tools. Chin. J. Aeronaut. 24 (4), 387–395.

ZARM Technik AG, 2020. 'Magnetic torquers [Online], Accessed August, 2020'. URL https://www.zarm-technik.de/#PRODUCTS.